Street canyon ventilation and airborne pollution dispersion: 2-D versus 3-D CFD simulations

Manuscript revised for Sustainable Cities and Society, 2019

Street canyon ventilation and air pollution dispersion: 2-D versus 3-D CFD simulations

Shuo-Jun Mei[abc], Zhiwen Luo[c*], Fu-Yun Zhao[ab*] Han-Qing Wang[d]

(a) School of Power and Mechanical Engineering, Wuhan University, Wuhan, Hubei Province, China

(b) Shenzhen Research Institute, Wuhan University, Shenzhen, Guangdong Province, China

(c) School of the Built Environment, University of Reading, Reading, United Kingdom

(d) School of Civil Engineering, University of South China, Hengyang, Hunan Province, China

* Corresponding author:

(1) Dr Zhiwen Luo, School of the Built Environment, University of Reading, United Kingdom; E-mail: z.luo@reading.ac.uk

(2) Prof. Fu-Yun Zhao, School of Power and Mechanical Engineering, Wuhan University, Wuhan, Hubei Province, China; E-mail: fyzhao@whu.edu.cn

Abstract

Urban ventilation is important for building a healthy urban living environment. 2-D CFD simulation has been used widely for street canyon ventilation due to its computational efficiency, but its applicability for a 3-D simulation has never been studied. This paper tried to answer the question: if and under what conditions, the widely-adopted 2-D CFD simulations on street canyon ventilation can represent real 3-D scenarios? 3-D simulations on street canyons with various street lengths and corresponding 2-D simulations are carried out with RNG k-ε model. Our study identified two important ventilation mechanism for controlling ventilation and dispersion in a 3-D street canyon, i.e., canyon vortex on the canyon top and the corner vortices at the street ends. The relative importance of these two driving forces will change with the street length/street width ratio (*B/W*). For isolated street canyon, when *B/W* is higher than 20 (for *H/W*=1) and 70 (*H/W*=2), the street canyon ventilation will be dominated by canyon vortex, and 3-D street canyon ventilation could be simplified as a 2-D case. For multiple street canyon, the threshold of *B/W* will become 20 when *H/W*=1, and 50 when *H/W*=2. The findings in this study could improve our approaches for simulating urban ventilation.

Keywords

CFD, Corner vortices, Street canyon, Urban ventilation

1. Introduction

A 'street canyon' refers to a narrow space between buildings that line up continuously along both sides of a street (Li et al., 2006). It has a unique climate where micro-scale meteorological processes dominate (Oke, 1988). Pollutants emitted at the ground level considerably deteriorate the local air quality and impose direct impacts on human health. The highest level of pollution and the most outdoor human activities are both concentrated at street canyons, causing the most serious health threat. (Vardoulakis et al., 2003). The

53 thermal comfort of pedestrians is also related to the street canyon geometries
54 (Chatzidimitriou and Yannas, 2013; Syafii et al., 2017). The pedestrian wind environment
55 and thermal comfort could be improved by intentionally designing the street canyon (Du
56 et al., 2019). Understanding the airflow and pollutant dispersion within the urban street
57 canyon is important to the sustainability of the urban environment.

58 The wind flows in the street canyons are inherently complex and exhibit a wide range
59 of physical characteristics including large low-speed areas, strong pressure gradients,
60 unsteady flow regions, three-dimensional effects and wakes (Deck, 2005). These wind
61 flow mechanisms are strongly related to geometry configurations and incoming wind
62 directions. The most widely studied cases in the literature are those with wind
63 perpendicular to the street axis because they represent the worst situation for air pollutant
64 dispersion (Li et al., 2006). Under such wind direction, it is reasonable to assume that the
65 street is infinitely long. Then, the original complex 3-D problem could be simplified as a
66 2-D one.

67 There are two types of 2D cases in previous studies: pure (only 2 directions are
68 simulated) and quasi 2D (all three directions are simulated for a quasi-infinitely long
69 street canyon using lateral periodic boundary conditions). In the 2-D cases, the most
70 important geometrical feature of a street canyon is the aspect ratio, which is the height
71 (H) of the canyon being divided by the width (W). Oke (1988) suggested that the flow
72 within 2-D street canyon could be described in terms of three regimes depending on the

aspect ratio (H/W) (Oke, 1988). From a three-dimensional point of view, the length (B), which usually expresses the road distance between two major intersections of the canyon, represents another important geometrical feature of the street canyon. The airflow in the street ends is characterized by horizontal corner vortices. Soulhac et al., (2009) concluded that the flow and dispersion at the street ends were dominated by a large vertical-axis recirculating vortex, which has an important influence on exchanges between the streets and overlying atmosphere. Carpentieri and Robins (2010) measured the mean and turbulent tracer fluxes within several street intersections in a wind tunnel model of a real urban area located in Central London. They found an increase in turbulent exchange at roof level at the intersections (Carpentieri et al., 2012). Their later wind tunnel measurements indicated that complex advective patterns appeared at intersections composed of very simple and regular geometries (Carpentieri et al., 2018). Michioka et al., (2014) conducted a series of large-eddy simulations of 3D street canyons with multiple street lengths. Their simulations show that the mean concentration within the canyon decreased with street length B due to stronger lateral dispersion. The DNS (direct numerical simulation) study of Coceal et al. (2014) showed that the complicated flow pattern had a significant influence on dispersion and mixing within the intersection. Based on the wind tunnel measurements, Nosek et al., (2017) calculated the pollution flux (turbulent and advective) at the lateral openings of three different 3D street canyons when the wind was perpendicular and oblique to the along-canyon axis. Their results confirmed

93 that the buildings' roof-height variability at the intersections plays an important role in
94 the dispersion of the traffic pollutants within 3D canyons.

95 Riain et al. (1998) summarized that the dispersion of gaseous pollutants in a street
96 canyon depended on the air exchange rate at the openings of street canyons, including the
97 roof of the street canyon and street ends. Vardoulakis et al. (2003) subdivided street
98 canyons into short ($B/H \approx 3$), medium ($B/H \approx 5$) and long canyons ($B/H \approx 7$) based on the
99 street length. In relatively short canyons, corner vortices might be strong enough to inhibit
100 the formation of a stable vortex perpendicular to the street in the mid-section. With the
101 increase of street length, this ventilation effect will become less important (Theurer,
102 1999). Chan et al. (2001) found that the B/H ratio can also affect the pollutant
103 concentration inside street canyons. Their later study found that the correlation between
104 pollutant concentration and B/H is due to the vortices generated at the street ends (Chan
105 et al., 2003). Xue and Li (2017) simulated the pollutant dispersion within 3D street
106 canyons and found a maximum pollutant concentration at the symmetry plane and
107 minimum pollutant concentration at street ends. All these important features which are
108 evident in 3-D street canyons are normally neglected in the 2-D airflow and ventilation
109 simulations. In LES studies, although 3-D computation domain is widely used, the streets
110 are usually assumed as infinitely long by using periodic boundary condition at side
111 boundaries to reduce computational cost (Lateb et al., 2016).

In the past two decades, there have been many modeling and experimental studies focusing on 2-D canyon cases (Magnusson et al., 2014； Ngan and Lo, 2016； Marciotto and Fisch, 2013； Koutsourakis et al., 2012). Previous studies show significant differences in airflow and dispersion between 3-D and 2-D canyons (Nosek et al., 2017; Xue and Li, 2017). However, it is still not clear when and how well the 2-D models could represent the airflow and pollutant dispersion in the 3D scenarios. As many urban design guidelines were based on previous studies with 2D model, it is necessary to find out the differences between 3D and 2D simulations. Additionally, the 2D simulation can extensively reduce the computational resource, especially at LES scenarios. In the near future, the quasi-2D model is expected to be widely used in LES studies. The present paper attempts to identify requirements that the ventilation at 3-D street canyon can be represented by 2-D models. Specifically, the main research questions are:

• Can a 2-D model represent a real 3-D street canyon for street canyon ventilation simulation?

• Is there a minimum street length/height ratio that a 2-D model could represent a 3-D street canyon?

These questions are explored by conducting a series of 3-D simulations with different street lengths and comparing against a corresponding 2-D simulation. The ambient wind is assumed perpendicular to the street direction at 3-D scenarios. Different indicators such as ACH, normalized concentration, retention time are used as metrics to evaluate the

ventilation and air pollution dispersion performance. This paper is structured as follows. The details of the model geometries and methodology are given in Section 2. In Section 3, the results are presented by looking at the flow and concentration fields along with multiple ventilation indices. Conclusions are presented in Section 4.

2. Methodology

The airflow in the urban area is considered as isothermal and the buoyancy effect is neglected. The time-averaged velocity and concentration fields are predicted using the Reynolds-averaged Navier–Stokes equations (RANS). The open source CFD (computational fluid dynamics) codes OpenFOAM v4.0 is used to solve governing equations of fluid dynamics. The data from wind tunnel experiments carried out by Tominaga and Stathopoulos (2011) is used to validate the computational model.

2.1. Domain dimensions

Figure 1 shows two types of street canyon model adopted here, including the isolated street canyon (ISC) and the multiple street canyon (MSC). Perret et al (2017) evaluated the large-scale unsteadiness of the shear layer separating from an upstream canyon edge on the vertical mass-exchange of the street canyon by wind tunnel measurement. It is suggested that the influence of the upstream buildings could not be simply ignored. Therefore, for the MSC configuration, we consider four canyons upstream and three canyons downstream of the target canyon. As the target canyon is far away from the flow separation at the leading edge, the airflow pattern at downstream canyons keeps unchanged (Mei et al., 2017). The width of the street canyons is fixed at $W = 0.1$ m, while the height of the buildings H varies to form different aspect ratios (H/W), i.e., H/W=1.0 and 2.0. All the cases considered fall into the skimming flow regime in the canyon (Oke, 1988). The building length B varies from $4W$ to $60W$ and the ambient wind blows perpendicular to the street canyon. The computational domain is selected based on the

best practice guidelines for CFD simulation of urban aerodynamics (Franke, 2007; Tominaga et al., 2008). The upstream distance and downstream distance are 5H and 15 H respectively. The domain height is 8H and the side distances are 5H. A passive pollutant is released at a line source at the centre of the street.

2.2. Boundary conditions

The inlet profiles are set based on the wind tunnel measurement of Tominaga and Stathopoulos (2011). The vertical profile of mean velocity in the approaching flow approximately obeys a power law with an exponent of 0.26. The upwind mean velocity U_{ref} at building height h (= W) is 3.8 m/s. A no-slip boundary condition is imposed at the building surfaces and the bottom boundary of the domain. The ground and building surface roughness are ignored in the simulation. The top and lateral boundaries of the domain are set as free-slip. On the outflow boundary, a zero diffusive flux is imposed for all flow variables in the direction normal to the outflow plane. This means that the conditions of the outflow plane are extrapolated from within the domain. This assumption is valid for fully developed flows.

2.3. Computational meshes

Unstructured hexahedral meshes are generated by snappyHexMesh (OpenCFD Ltd, v4.0) using the cutCell assembly meshing function. The domain near the buildings and ground contains the smallest grids, cubic cells with dimensions of $0.05W \times 0.05W \times 0.05W$. To reduce the computational load, sparser grids are used in the regions away from the buildings and ground. The largest cubic cells are with dimensions of $0.2W \times 0.2W \times 0.2W$. The total number of grids ranges from 0.6 to 7.8 million, depending on buildings' length B and canyon number.

The grid-independency test was conducted by comparing three types of mesh (coarse, basic and refined mesh) for the single canyon case with $B/W = 4$. The coarse and refined meshes were built by reducing and increasing the mesh number between buildings by 1.5 times, respectively. The mean velocity and turbulent kinetic energy (TKE) at the middle

line (along *y*-direction) at the roof of street canyon calculated between three meshes are compared in Fig. 2. By further increasing the mesh number (from basic to refined mesh), both velocity and turbulent kinetic energy (TKE) fields showed little changes, which shows that the present grid is sufficiently dense for the present studies.

2.4. Solution method

The atmospheric air can then be assumed incompressible. In 2-D RANS modeling, the flow properties are disintegrated into their mean and fluctuating components by Reynolds decomposition and substituted in the Navier–Stokes equations, which could be written as:

$$\frac{\partial \overline{u_i}}{\partial x_i} = 0 \tag{1}$$

$$\frac{\partial \overline{u_i}}{\partial t} + \frac{\partial}{\partial x_j}(\overline{u_i}\,\overline{u_j}) = -\frac{\partial \overline{p}}{\partial x_i} + \frac{\partial}{\partial x_i}(\overline{\tau_{ij}} - \overline{u_i' u_j'}) \tag{2}$$

where x_i are the Cartesian coordinates. The mean and fluctuating components of flow properties are marked with overbar and apostrophe respectively. For example, $\overline{u_i}$ represents the components of the mean velocity. Here, $\overline{p}$ is the pressure, $\overline{u_i' u_j'}$ the Reynolds stress tensor which remains after the hydrostatic pressure is removed. The Reynolds stress tensor appearing in the mean momentum equation is modeled using the Boussinesq's eddy viscosity model:

$$-\overline{u_i' u_j'} = 2\nu_t \overline{S_{ij}} - \frac{2}{3} k \delta_{ij} \tag{3}$$

where the strain rate tensor $\overline{S_{ij}} = \frac{1}{2}\left(\frac{\partial u_i}{\partial x_j} + \frac{\partial u_j}{\partial x_i}\right) - \frac{1}{3}\left(\frac{\partial u_i}{\partial x_i}\right)\delta_{ij}$, k denotes the turbulent kinetic energy and ν_t the turbulent viscosity. The RNG k-ε model (Yakhot and Orszag,

1986) is selected due to its generally good performance in predicting flow around buildings (Tominaga and Stathopoulos, 2010). The steady transport equation for the time-averaged pollutant concentration ($\bar{c}$, kg/ m^3) is:

$$\overline{u_j}\frac{\partial \bar{c}}{\partial x_j} = \frac{\partial}{\partial x_j}(K_c \frac{\partial \bar{c}}{\partial x_j}) + Q \quad (4)$$

where $\overline{u_j}$ is the time-averaged velocity components, Q is the pollutant emission rate, $K_c = \nu_t/S_{ct}$ is the turbulent eddy diffusivity of pollutants, ν_t is the kinematic eddy viscosity, $S_{ct} = 0.7$ is the turbulent Schmidt number (Di Sabatino et al., 2007).

All transport equations are discretized using a finite volume method. The hybrid second order upwind/central differencing scheme is utilized to discretize the advection terms, with an option of the second-order upwind scheme and the QUICK scheme (Patankar, 1980). The discretized differential equations are solved by the SIMPLE algorithm (Patankar, 1980), which is solved by simpleFOAM solver in OpenFOAM .

Convergence is achieved when all scaled residuals are less than 10^{-5} and the average flow speeds at several locations.

2.5. Model validation

Model validation is essential for CFD studies before further analysing. The accuracy of the current CFD model is demonstrated by comparing to the experimental database obtained from the wind tunnel at Niigata Institute of Technology (Tominaga and Stathopoulos, 2011). The three-dimensional canyon was characterized with $H/W = 1.0$ and $H/B = 0.5$. Ethylene (C_2H_4) was used as a tracer gas and released at the centre of the street bottom with a concentration of 1000 ppm. The pollutant was released by a point source in their experiment. The atmospheric boundary flow profiles were produced by a combination of spires and surface roughness in their experiment. The velocity and turbulent profiles could be represented by $U(z) = U_{ref}(z/H)^{0.26}$. $k(z) = (U(z)I(z))^2$,

230 $\varepsilon = \sqrt{C_\mu} k(z) \frac{dU(z)}{dz}$, according to their measurement. The inlet profiles have been
231 compared to the measurement of Tominaga and Stathopolous (2011) in Fig. 3. Here,
232 U_{ref} = 3.8 m/s. C_μ = 0.0845, is a constant in the RNG turbulent model, $I(z)$ is the turbulent
233 intensity.

234 The velocity vectors on the vertical and horizontal planes were compared with the wind
235 tunnel experiment in Figs. 4a and 4b. On the vertical section at the middle point, a single
236 recirculation flow was observed in the street canyons. On a horizontal section at z/H =
237 0.1, two vortices appeared within the street canyons. The general patterns of the
238 recirculation flow in CFD were close to that in the experiment. Figure 4d, 4e and 4f
239 compared the measured and calculated concentration $\bar{c}$ along the streamwise direction
240 (x). Overall, the CFD prediction of $\bar{c}$ is satisfactory. Despite overestimation is found at
241 the height of z/H = 0.1, it is consistent with previous RANS simulations (Gromke et al.,
242 2008; Tominaga and Stathopoulos, 2011). These differences were caused by
243 underestimated turbulence diffusions in lateral direction in RANS models.

244 In order to evaluate the predictions of a model with experimental observations, the
245 normalized mean square error (*NMSE*) recommended by Hanna et al. (1991) were used,
246 which represents the normalized discrepancy between the computed and experimental
247 values and is calculated as follows,

248 $$NMSE = \frac{\sum_{i=1}^{n} (O_i - P_i)^2}{\sum_{i=1}^{n} (O_i P_i)} \quad (5)$$

249 where n represents the number of points, O_i represents the measurements at each point
250 and $\overline{O}$ is the measurement mean. P_i and $\overline{P}$ represent the computed values and the
251 corresponding mean at each point, respectively. A perfect model could have the
252 parametric values of *NMSE* = 0.0. According to the recommended criteria by COST

Action 732 (Efthimiou et al., 2011), 'state of the art' model performance has met the following statistical metrics standard: NMSE < 1.5. The calculated *NMSE* at the bottom line, middle line and top line are 0.128, 0.182 and 0.412, respectively. As the focus of the present study is on evaluating the difference in pollutant dispersion between two-dimensional and three-dimensional RNAS models, the numerical model used in this study is considered reliable.

3. Results and discussion

3.1. Three-dimensional street canyon airflow

Dispersion within three-dimensional street canyon is heavily influenced by the flow structure. Therefore, we begin by describing the basic flow pattern within a street canyon surrounded by urban buildings and subjected to perpendicular approaching wind, as shown in Fig. 5. Gromke and Ruck (2007) summarized that there are two distinguishable flow characteristics, i.e., vertically rotating (recirculating with the along-canyon axis) canyon vortices and horizontally rotating (recirculating with the vertical axis) corner eddies. The canyon vortices are driven by shear forces of the skimming flow above the rooftop. Instead, the corner vortices are driven by the shear at street ends, which is induced by the channelling flow. The resulting flow in a 3-D street canyon could be more complex due to the interaction between the corner vortices and canyon vortices. Becker et al. (2002) and Kim and Baik (2004) found a portal vortex behind the upwind building, which extends toward the lower edges of the downwind building.

The flow structure is depicted by tracing a set of streamlines originated from multiple seed locations on a straight line above the line source (z/H = 0.1), shown in Fig. 6. The streamlines are coloured by mean velocity. Here, cases with B/W = 4 are selected for illustration. The basic characteristics described by Gromke and Ruck (2007) are also

found in streamlines. However, for the ISC configuration, the corner vortices extend beyond the street ends toward the upwind corner. This is because of the reverse flow near the side walls induced by the flow separation (Murakami and Mochida, 1989). In contrast, the corner vortices are well confined within the canyon volume in the MSC configuration. This is because the target canyon is far away from the leading building and not influenced by the flow separation. The $y/B = 0$ planes represent the symmetrical planes and $y/B = \pm 0.5$ represent the street ends.

The x-velocity was filtered as zero to transfer the 3D streamlines to 2D streamlines. The 2D streamlines in the ISC case ($B/W = 4$) were plotted at planes parallel to the street direction to show the flow structure along the street direction. The planes were located at the centrelines of the streets, shown as Fig. 7. A counter-rotating flow structure was observed at the y-z plane. This flow structure induced ambient air from the street ends into the street canyon volume. The inlet flows at two street ends were of opposite directions and collided at the symmetry plane, resulting with an upward flow.

It is interesting to note that mean streamlines escapes from the canyon roof at the symmetrical planes, instead of recirculating below roof level. When the streamlines recirculate below the roof level, the pollutant is transported mainly due to turbulence (Buccolieri et al., 2009). However, the mean upward flow extended beyond the roof level could extensively raise the mass transfer rate. Fig. 8 shows contours plots of the normalized vertical velocity w^* ($= w/U_{ref}$, where w is the mean vertical velocity) at two different height $z = 0.1H$ and $z = 1.0H$. Strong upward flow is observed at both heights. The upward flow is confined within a narrow area adjacent to the upwind buildings except at the symmetrical planes, where the upward flow extends across the whole street canyon width. This indicates that pollutants may be transferred directly from ground level to roof level at symmetrical planes (refers to the x-z plane at $y = 0$). This statement could be supported by abnormal pollutant concentration decay at that position, which is also observed in previous wind tunnel experiment (Gromke, 2011; Gromke and Ruck, 2012)

and CFD simulations (Jeanjean et al., 2015). In fact, the concentration drop in the symmetry plane is not common in previous studies. There are several reasons: 1) the point sources instead of line sources were used in previous 3D street canyon studies; 2) the concentration drops were only observed at specific street length range; when street is long enough, the concentration drop is no longer obvious, as shown as Fig. 15. 3) the surrounding buildings (with intersections) are ignored in the present studies, which could potentially suppress the horizontal convergence flow, as shown in Fig. 7

3.2. Pollutant dispersion at the three-dimensional street canyon

To facilitate the comparison among the 2-D and 3-D simulations, dimensionless concentration C is introduced as a function of the simulated pollutant concentration $\bar{c}$ (kg/m^3), reference wind speed U_{ref} (m/s), height of the building H (m), length of the line source B (m), and ethane flow rate Q (kg/s) (Meroney et al., 1996),

$$C = \frac{\bar{c} U_{ref} HB}{Q} \tag{6}$$

The dimensionless concentration fields at three x-z planes of 3-D street canyons along with the corresponding 2-D cases are shown in Fig. 9 and Fig. 10. Generally, the concentration distributions in these planes of 3-D simulation are different than those in the case of the 2D canyon. The concentration levels are appreciably lower at y/B = 0 planes, which is due to strong upward flow as described in the former section. The pollutant concentration are even lower at the y/B = 0.45 planes, where are close to the street ends. The corner vortices at street ends could significantly enhance the local dilution rate (Buccolieri et al., 2009). An appreciably higher concentration is observed at the street level at y/B = 0.25 planes, which is quite different from 2-D canyon. This indicates the convergence flow along the street direction has non-negligible influence on the pollutant dispersion. These differences remain at the very long street (B/W = 60). It

should be cautious when applying 2-D model to predict the pollutant distribution in street canyon

3.3 Ventilation in the street canyon

The pollutant dilution at the 2-D street canyon is governed by the air exchange at roof level, while for the 3-D street canyon, ventilation both at the roof level and street ends will play its role. The averaged ACH_{roof} (Hang and Li, 2010) is used to evaluate the air exchange at the street canyon roof, which is divided into the mean component:

$$\overline{\mathrm{ACH}}_{roof} = \frac{1}{HBW} \int_{\Gamma_{roof}} \overline{\mathrm{w}}_{+} dxdy \,, \tag{7}$$

and the turbulent component:

$$ACH'_{roof} = \frac{1}{HBW} \int_{\Gamma_{roof}} \frac{1}{2} \sqrt{\overline{w'w'}} dx = \frac{1}{HBW} \int_{\Gamma_{roof}} \sqrt{[\frac{k}{6} - \frac{1}{2} \nu_t (\frac{\partial \overline{w}}{\partial z})]} dxdy \,, \tag{8}$$

where w is the vertical velocity component, ν_t the turbulent viscosity and Γ_{roof} the roof area of the street canyon. The subscript + signifies that only the upward velocity $w > 0$ (i.e., air removal) is considered.

Similarly, the ACH_{side} at street ends is calculated as:

$$\overline{\mathrm{ACH}}_{side} = \frac{1}{HBW} \int_{\Gamma_{side}} \overline{\mathrm{v}}_{+} dxdz \tag{9}$$

$$ACH'_{side} = \frac{1}{BHW} \int_{\Gamma_{side}} \frac{1}{2} \sqrt{\overline{v'v'}} dx = \frac{1}{BHW} \int_{\Gamma_{side}} \sqrt{[\frac{k}{6} - \frac{1}{2} \nu_t (\frac{\partial \overline{v}}{\partial y})]} dxdz \tag{10}$$

where v is the velocity ay y-direction component and Γ_{side} the street ends area of the street canyon. The subscript + signifies that only the outward velocity $v > 0$ (i.e., air removal) is considered. It should be noted that the v_+ for one street end and v_- for the opposite street end. The total ventilation for street canyon ACH_c will be the sum of ACH_{roof} and ACH_{side}

$$ACH_c = ACH_{roof} + ACH_{side} \tag{11}$$

The air exchange rate and its mean and turbulent components at canopy roof as a function of the street length are presented at Fig. 11. The *ACH* at 2-D simulations is plotted as blue lines. It is found that the ACH_{roof} contributed by mean flow is smaller than turbulent fluctuation for all cases. In the MSC configuration, the mean flows in that configuration are parallel to the roof surfaces, resulting with weak mean vertical flow. Therefore, the turbulent fluctuation (ACH'_{roof}) dominants the air exchange at roof level. Compared to the MSC configuration, the mean flow in the ISC configuration plays a more significant role in the air exchange due to flow separation. It was found that ACH_{roof} were almost unchanged with the increase of street length when streets were long enough. However, the variation trend varies from case to case. For isolated canyon with H/W = 1.0, the ACH_{roof} increases significantly with the street length. When we increase the H/W to 2.0 at isolated canyon cases, the ACH_{roof} decreases firstly before increases monotonically. This could be due to the flow separation at street ends, which may decrease the shear at roof level.

The air exchange rate and its mean and turbulent components at street ends as a function of the street length are presented at Fig. 12. In contrast to street canyon roof, the ACH_{side} has a negative relation with the street length. This explained why there is a peak value for the ACH_c. The functions between the ACH_c and street length are plotted in Fig. 13. When initially increasing the street length, the decrease of *ACH* at street ends plays a dominant role. As a result, the total *ACH* increases with the street length. When further increasing the street length, the increase of the *ACH* at street roof plays a dominant role. Therefore, the total *ACH* decreases with the street length when B/W is longer than 30.

As shown in the flow field at Fig. 6 and Fig. 7, the street length has two opposite effects on the pollutant dispersion. Firstly, with the increase of the street length, the corner vortices have less impact on the pollutant dilution of the whole canyon volume. As a result, the pollutant concentration increased with street length. Secondly, the interaction between the corner vortices and canyon vortices would also be weakened when increasing

the street length. As a result, the pollutant concentration would decrease with street length. With continue increasing the street length, the first effect dominants the pollutant dilution and the second one gradually disappears.

3.4. Retention time at street canyon

The ventilation performance of the whole canyon will be evaluated by the canyon retention time τ_c (Cheng et al., 2008), calculated as:

$$\Theta = \frac{1}{V}\int\int\int c dx dy dz \tag{12}$$

$$\tau_c = \frac{\Theta \times V}{Q} \tag{13}$$

where c is the local concentration of a passive tracer gas (kg/m^3), and Q is the pollutant emission rate (kg/s)), V the volume of the street canyon. The average pollutant concentration Θ signifies the overall air quality of the street canyon while τ_c represents the time scale for a parcel of pollutant being removed from the street canyon.

Figure 14 shows the canyon retention time as a function of the street length. The canyon retention time of 2-D simulation is plotted as blue dash lines. The most important goal for the present study is to find the minimum street length that 2-D simulation can represent the ventilation of 3-D street canyon. In ISC configuration, the minimum street lengths are 20W and 70W for H/W = 1.0 and 2.0 respectively. In MSC configuration, the minimum street lengths are 20W and 50W for H/W = 1.0 and 2.0 respectively.

The canyon retention time increases firstly and then decreases to a constant value with the increasing street length. Additionally, the peak value increases with the aspect ratio (H/W). In the ISC configuration, the canyon retention time reaches its maximum value at B/W = 6 for H/W = 1.0 and at B/W = 20 for H/W = 1.0. In the MSC configuration, the maximum value of retention time corresponds to B/W = 8 and 20 for H/W = 1.0 and 2.0, respectively. This is just opposite to variation of the total *ACH*, which indicates that the air exchange at street openings dominates the pollutant dilution at these cases.

405 In order to show the integrated characteristics of the canopy layer, we average the above
406 quantities inside the street canyon, i.e.

407 $\Omega_{canyon} = \{(x, z) : -0.5W \le x \le 0.5W,\ -0.5B \le y \le 0.5B,\ 0 \le z \le H\}$:

408 $$\bar{\varphi} = \frac{B}{QWH} \int_{-0.5W}^{0.5W} \int_{0}^{H} c(x, z) dx dz \tag{14}$$

409 In other words, $\bar{\varphi}$ denotes an average retention time along the *y*-direction.

410 Figure 15 shows the distribution of retention time along the street direction (*y*-
411 direction). For the ISC configuration with *H*/*W* =1.0, the retention time decreases
412 significantly at the street end, indicating the corner vortices enhanced local dilution rate.
413 Toward the symmetrical planes, the retention time rises rapidly before significant
414 declining in a narrow zone at the symmetrical planes. As explained before, pollutants
415 could be transferred directly from ground level to roof level at symmetrical planes. With
416 the increase of street length, the rise of retention time disappears at symmetrical planes.
417 This indicates that the increase in retention time is caused by interaction between canyon
418 vortex and corner vortices.

419 For the ISC configuration with *H*/*W* =2.0, a significant increase of local retention time
420 is found at the street ends. It could be caused by the of corner vortices, which can become
421 more strength at the deep street canyon. However, the increase of retention time at street
422 ends is not found in multiple canyon cases. This suggests that the corner vortices are not
423 driven by shear force at street ends as suggested by Gromke and Ruck (2007). Instead,
424 they are resulted from flow separation at side walls. Such difference could be due to the
425 fact that the skimming flow regime is chosen in the present study.

426 **3.5 Limitations**

427 Although the present RANS model provides satisfactory accuracy, the unsteadiness of
428 the turbulence could not be reproduced. Studies with LES or DNS model are still
429 expected, which could provide more information about the turbulent fluctuation.
430 Moreover, in some previous studies (e.g., Soulhac et al. (2009), Michioka et al. (2014)),

that the spatially averaged concentration is the highest at this central plane. In other studies, abnormal concentration decay was found at the central plane (Gromke, 2011; Gromke, and Ruck, 2012). Although we have made some new insight on this issue, there is also a clear need for a set of wind tunnel experimental studies in the future to support our observations. It should also be noted that isolated street canyons instead of street canyons embodied in an urban street network were analysed here. The local flow characteristics could also be affected by surrounding buildings especially intersections.

4. Conclusions

In this study, the differences between 2-D and 3-D RANS simulations on resolving the ventilation at street canyon are investigated. The focus is on identifying the threshold value of street length (B) that 2-D results can well represent real 3-D street canyon. Here the skimming flow regime is considered with two aspect ratios (H/W = 1.0 and 2.0) for their wide adoption in previous studies. Both isolated street canyon (ISC) and multiple street canyon (MSC) configurations are considered. The air exchange rate and pollutant retention time are used to evaluate the ventilation and pollution dispersion inside the street canyon.

With the increase of street length, the differences in ventilation between 3-D and 2-D simulation become insignificant, although there still exists a minor difference between them. A narrow zone with strong upward flow is found at the symmetrical planes at the leeward wall of the street canyon, where an enhanced ventilation is observed. The interaction between this upward flow and vertically rotating vortices at street ends leads to the distinctions between the 3-D and 2-D simulations.

With the increase of street length, the averaged retention time of 3-D simulation approaches 2-D simulation. The differences in retention time between 2-D and 3-D simulations disappear when B/W is larger than 20 for H/W = 1.0 and 70 for H/W = 2.0. In

457 the MSC configuration, the differences disappear when B/W is larger than 20 for H/W =
458 1.0 and 50 for H/W = 2.0.

459 The correlation between the street length and ventilation capacity could be used in
460 optimizing the urban street design to achieve better air quality. For example, the street
461 length with maximum pollutant accumulation should be avoided in urban design.
462 Additionally, this study could be used in locating the monitoring point for air quality
463 measurement in the street canyons. Monitoring facilities installed in street ends will
464 underestimate the air pollution and overestimate the air pollution at central points.

465

466 **Acknowledgments**

467 The first author wishes to acknowledge the financial support from Wuhan University.
468 Prof. Fu-Yun Zhao would also like to acknowledge the financial support from the Natural
469 Science Foundation of China (NSFC Grant No. 51778504), Fundamental Research
470 Projects from Shenzhen Government (Grant No. JCYJ20160523160857948), and
471 National Key Research and Development Program of the Ministry of Science and
472 Technology of China (Grant No. 2018YFC0705201, Grant No. 2018YFB0904200).

473

474 **References**

475 Becker, S., Lienhart, H., Durst, F., 2002. Flow around three-dimensional obstacles in
476 boundary layers. Journal of Wind Engineering and Industrial Aerodynamics 90, 265-
477 279.

478 Buccolieri, R., Gromke, C., Di Sabatino, S., Ruck, B., 2009. Aerodynamic effects of trees
479 on pollutant concentration in street canyons. Science of The Total Environment 407,
480 5247-5256.

481 Carpentieri, M., Robins, AG., 2010. Tracer flux balance at an urban canyon intersection.
482 Boundary-layer meteorology 135(2), 229-242.

Carpentieri, M., Hayden, P., Robins, AG., 2012. Wind tunnel measurements of pollutant turbulent fluxes in urban intersections. Atmospheric Environment 46, 669-674.

Carpentieri, M., Robins, AG., Hayden, P., Santi, E., 2018. Mean and turbulent mass flux measurements in an idealised street network. Environmental pollution 234, 356-367.

Chan, A.T., Au, W.T.W., So, E.S.P., 2003. Strategic guidelines for street canyon geometry to achieve sustainable street air quality—part II: multiple canopies and canyons. Atmospheric Environment 37, 2761-2772.

Chan, A.T., So, E.S., Samad, S.C., 2001. Strategic guidelines for street canyon geometry to achieve sustainable street air quality. Atmospheric Environment 35, 4089-4098.

Chatzidimitriou, A., Yannas, S., 2017. Street canyon design and improvement potential for urban open spaces; the influence of canyon aspect ratio and orientation on microclimate and outdoor comfort. Sustainable cities and society 33, 85-101.

Cheng, W.C., Liu, C.H., Leung, D.Y.C., 2008. Computational formulation for the evaluation of street canyon ventilation and pollutant removal performance. Atmospheric Environment 42, 9041-9051.

Coceal, O., Goulart, E.V., Branford, S., Glyn Thomas, T., Belcher, S.E., 2014. Flow structure and near-field dispersion in arrays of building-like obstacles. Journal of Wind Engineering and Industrial Aerodynamics 125, 52-68.

Deck, S., 2005. Zonal-Detached-Eddy Simulation of the Flow Around a High-Lift Configuration. AIAA Journal 43, 2372-2384.

Di Sabatino, S., Buccolieri, R., Pulvirenti, B., Britter, R., 2007. Simulations of pollutant dispersion within idealised urban-type geometries with CFD and integral models. Atmospheric Environment 41(37), 8316-8329.

Du, Y., Mak, CM., Li, Y., 2019. A multi-stage optimization of pedestrian level wind environment and thermal comfort with lift-up design in ideal urban canyons. Sustainable Cities and Society 101424.

509 Efthimiou, G., Santiago, J., Martilli, A., 2011. COST 732 in Practice: the MUST
510 ModelEvaluation Exercise.
511 Franke, J., et al., 2007. The COST 732 Best Practice Guideline for CFD simulation of
512 flows in the urban environment: a summary. International Journal of Environment
513 and Pollution 44.1.
514 Gromke, C., Buccolieri, R., Di Sabatino, S., Ruck, B., 2008. Dispersion study in a street
515 canyon with tree planting by means of wind tunnel and numerical investigations –
516 Evaluation of CFD data with experimental data. Atmospheric Environment 42,
517 8640-8650.
518 Gromke, C., Ruck, B., 2007. Influence of trees on the dispersion of pollutants in an urban
519 street canyon—Experimental investigation of the flow and concentration field.
520 Atmospheric Environment 41, 3287-3302.
521 Gromke, C., 2011. A vegetation modeling concept for building and environmental
522 aerodynamics wind tunnel tests and its application in pollutant dispersion studies.
523 Environmental Pollution 159(8-9), 2094-2099.
524 Gromke, C., Ruck, B., 2012. Pollutant concentrations in street canyons of different aspect
525 ratio with avenues of trees for various wind directions. Boundary-Layer
526 Meteorology, 144(1), 41-64.
527 Hanna, S.R., Strimaitis, D.G., Chang, J.C., 1991. Hazard Response Modelling
528 Uncertainty (A Quantitative Method) Volume II. Evaluation of Commonly-used
529 Hazardous Gas Dispersion Model, Report F08635-89-C-0136, Sigma Research
530 Corporation, Air Force Engineering andService Center, Tyndal Air Force Base
531 Florida, pp. 338.
532 Hang, J., Li, Y., 2010. Wind conditions in idealized building clusters: macroscopic
533 simulations using a porous turbulence model. Boundary-layer meteorology 136,
534 129-159.

535 Jeanjean, A. P., Hinchliffe, G., McMullan, W. A., Monks, P. S., Leigh, R.J., 2015. A CFD
536 study on the effectiveness of trees to disperse road traffic emissions at a city scale.
537 Atmospheric Environment 120, 1-14.
538 Kim, J.-J., Baik, J.-J., 2004. A numerical study of the effects of ambient wind direction
539 on flow and dispersion in urban street canyons using the RNG k-ε turbulence model.
540 Atmospheric Environment 38, 3039-3048.
541 Koutsourakis, N., Bartzis, J.G., Markatos, N.C., 2012. Evaluation of Reynolds stress, k-
542 epsilon and RNG k-epsilon turbulence models in street canyon flows using various
543 experimental datasets. Environmental Fluid Mechanics 12, 379-403.
544 Lateb, M., Meroney, R.N., Yataghene, M., Fellouah, H., Saleh, F., Boufadel, M.C., 2016.
545 On the use of numerical modelling for near-field pollutant dispersion in urban
546 environments − A review. Environmental Pollution 208, 271-283.
547 Li, X.-X., Liu, C.-H., Leung, D.Y., Lam, K., 2006. Recent progress in CFD modelling of
548 wind field and pollutant transport in street canyons. Atmospheric Environment 40,
549 5640-5658.
550 Magnusson, S., Dallman, A., Entekhabi, D., Britter, R., Fernando, H.J.S., Norford, L.,
551 2014. On thermally forced flows in urban street canyons. Environmental Fluid
552 Mechanics 14, 1427-1441.
553 Marciotto, E.R., Fisch, G., 2013. Wind tunnel study of turbulent flow past an urban
554 canyon model. Environmental Fluid Mechanics 13, 403-416.
555 Mei, S.-J., Hu, J.-T., Liu, D., Zhao, F.-Y., Li, Y., Wang, Y., Wang, H.-Q., 2017. Wind
556 driven natural ventilation in the idealized building block arrays with multiple urban
557 morphologies and unique package building density. Energy and Buildings 155, 324-
558 338.
559 Meroney, R.N., Pavageau, M., Rafailidis, S., Schatzmann, M., 1996. Study of line source
560 characteristics for 2-D physical modelling of pollutant dispersion in street canyons.
561 Journal of Wind Engineering and Industrial Aerodynamics 62, 37-56.

562 Michioka, T., Takimoto, H., Sato, A., 2014. Large-eddy simulation of pollutant removal
563 from a three-dimensional street canyon. Boundary-layer meteorology 150(2), 259-
564 275.
565 Murakami, S., Mochida, A., 1989. Three-dimensional numerical simulation of turbulent
566 flow around buildings using the *k*-ε turbulence model. Building and Environment
567 24, 51-64.
568 Ngan, K., Lo, K.W., 2016. Revisiting the flow regimes for urban street canyons using the
569 numerical Green's function. Environmental Fluid Mechanics 16, 313-334.
570 Nosek, Š., Kukačka, L., Jurčáková, K., Kellnerová, R., Jaňour, Z., 2017. Impact of roof
571 height non-uniformity on pollutant transport between a street canyon and
572 intersections. Environmental Pollution 227, 125-138.
573 Oke, T.R., 1988. Street design and urban canopy layer climate. Energy and buildings 11,
574 103-113.
575 Patankar, S., 1980. Numerical heat transfer and fluid flow. CRC Press.
576 Perret, L., Blackman, K., Fernandes, R., Savory, E., 2017. Relating street canyon vertical
577 mass-exchange to upstream flow regime and canyon geometry. Sustainable cities
578 and society 30, 49-57.
579 Riain, C.M., Fisher, B., Martin, C.J., Littler, J., 1998. Flow Field and Pollution Dispersion
580 in a Central London Street. Environmental Monitoring and Assessment 52, 299-314.
581 Soulhac L, Garbero V, Salizzoni P, et al. Flow and dispersion in street intersections [J].
582 Atmospheric Environment, 2009, 43(18): 2981-2996.
583
584 Syafii, NI., Ichinose, M., Kumakura, E., Jusuf, SK., Chigusaa, K., Wong, NH., 2017.
585 Thermal environment assessment around bodies of water in urban canyons: A scale
586 model study. Sustainable cities and society 34, 79-89.
587 Theurer, W., 1999. Typical building arrangements for urban air pollution modelling.
588 Atmospheric Environment 33, 4057-4066.

589 Tominaga, Y., Mochida, A., Yoshie, R., Kataoka, H., Nozu, T., Yoshikawa, M.,
590 Shirasawa, T., 2008. AIJ guidelines for practical applications of CFD to pedestrian
591 wind environment around buildings. Journal of Wind Engineering and Industrial
592 Aerodynamics 96, 1749-1761.
593 Tominaga, Y., Stathopoulos, T., 2010. Numerical simulation of dispersion around an
594 isolated cubic building: Model evaluation of RANS and LES. Building and
595 Environment 45, 2231-2239.
596 Tominaga, Y., Stathopoulos, T., 2011. CFD modeling of pollution dispersion in a street
597 canyon: Comparison between LES and RANS. Journal of Wind Engineering and
598 Industrial Aerodynamics 99, 340-348.
599 Vardoulakis, S., Fisher, B.E., Pericleous, K., Gonzalez-Flesca, N., 2003. Modelling air
600 quality in street canyons: a review. Atmospheric environment 37, 155-182.
601 Xue, F., Li, X., 2017. The impact of roadside trees on traffic released PM10 in urban
602 street canyon: Aerodynamic and deposition effects. Sustainable cities and society
603 30, 195-204.
604 Yakhot, V., Orszag, S.A., 1986. Renormalization-group analysis of turbulence. Physical
605 review letters 57, 1722.
606

Figures and tables

Figure 1

`

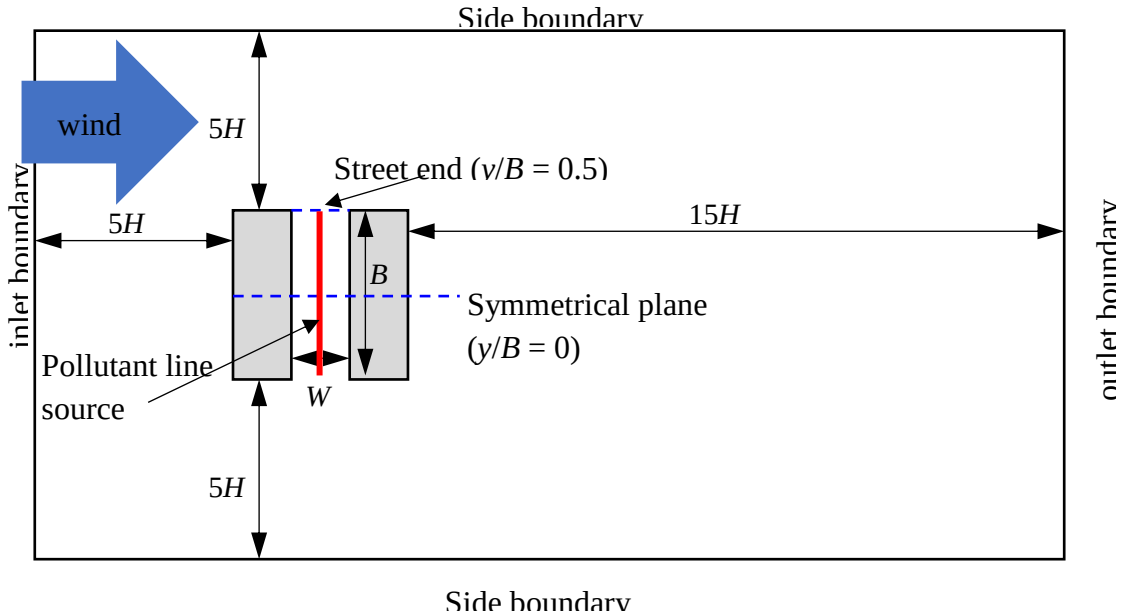

(a)

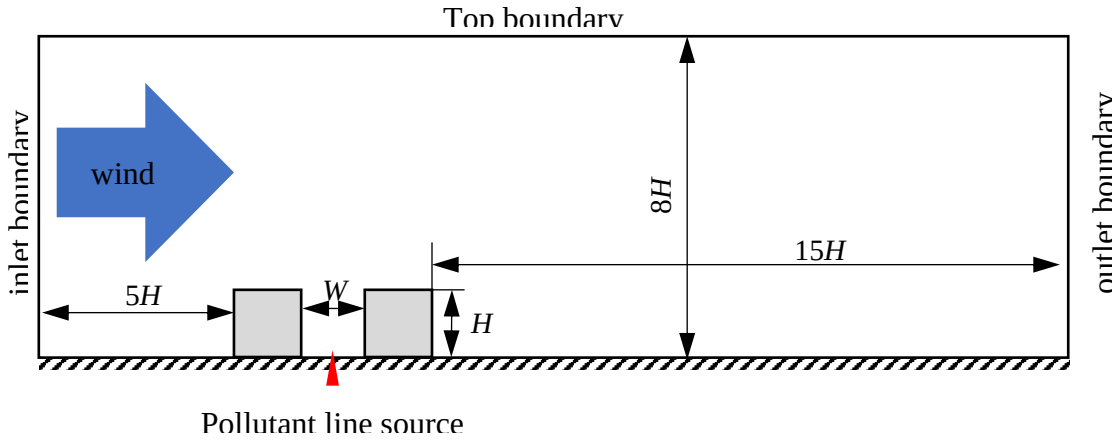

(b)

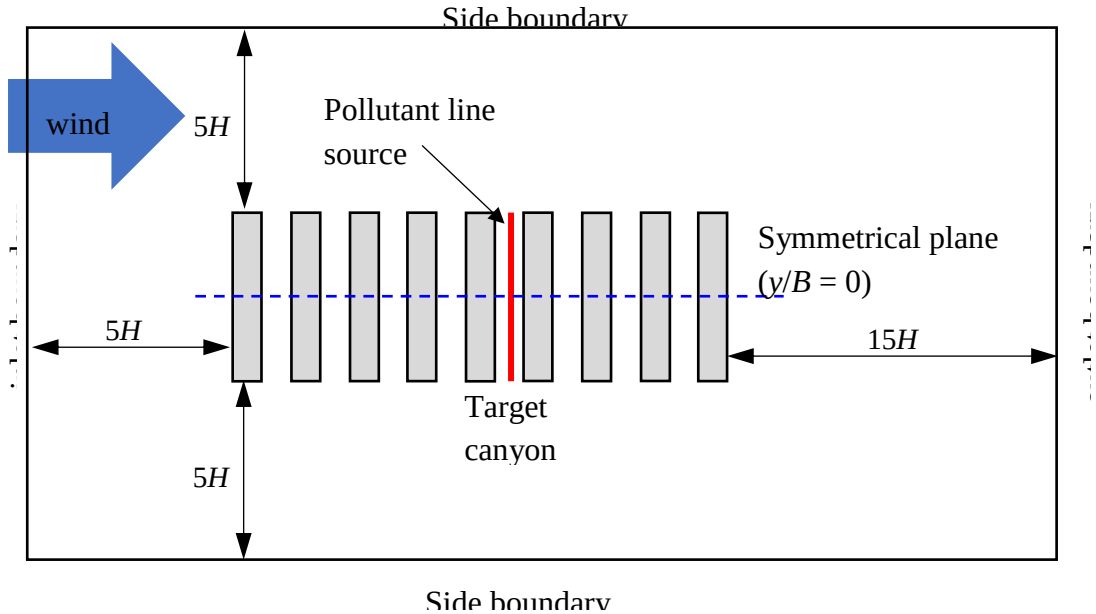

(c)

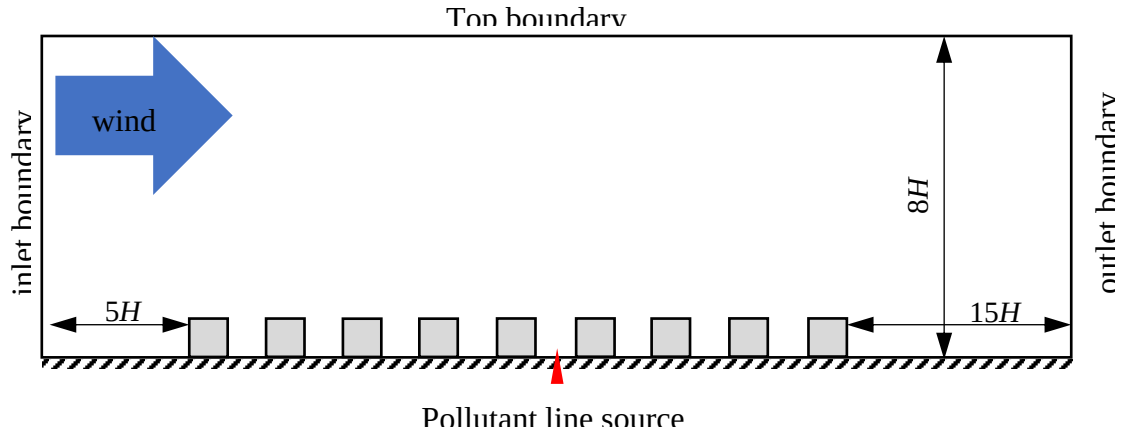

(d)

Fig. 1. Schematic view of computational domains used in CFD studies: (a) top view for isolated canyon and (b) side view for isolated canyon configuration, (c) top view for multiple canyons and (d) side view for multiple canyons configuration.

Figure 2

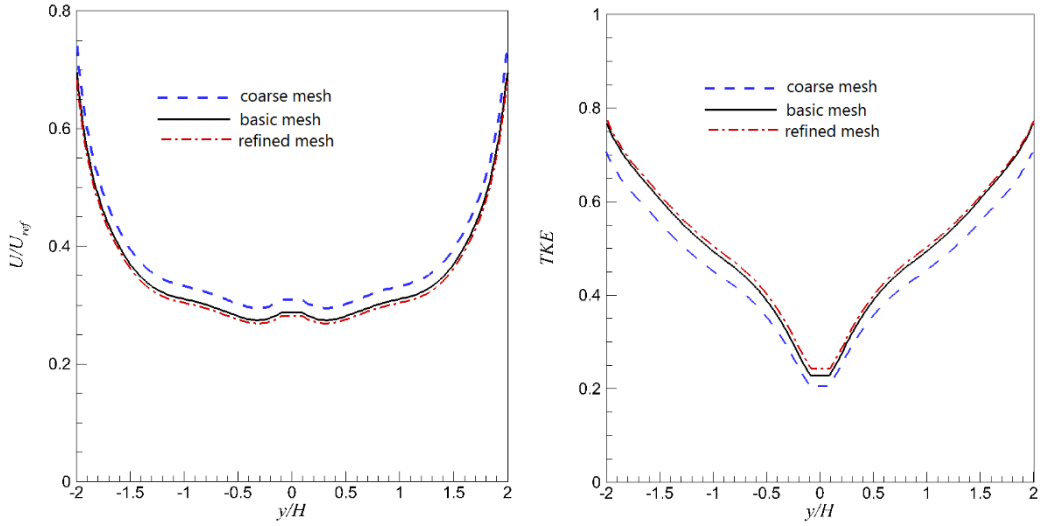

Fig. 3. Comparison of mean velocity (a) and turbulent kinetic energy (TKE) (b) at middle line (along *y*-direction) at the roof of single canyon case with $B/W = 4$.

654 Figure 3
655
656
657
658
659
660
661
662

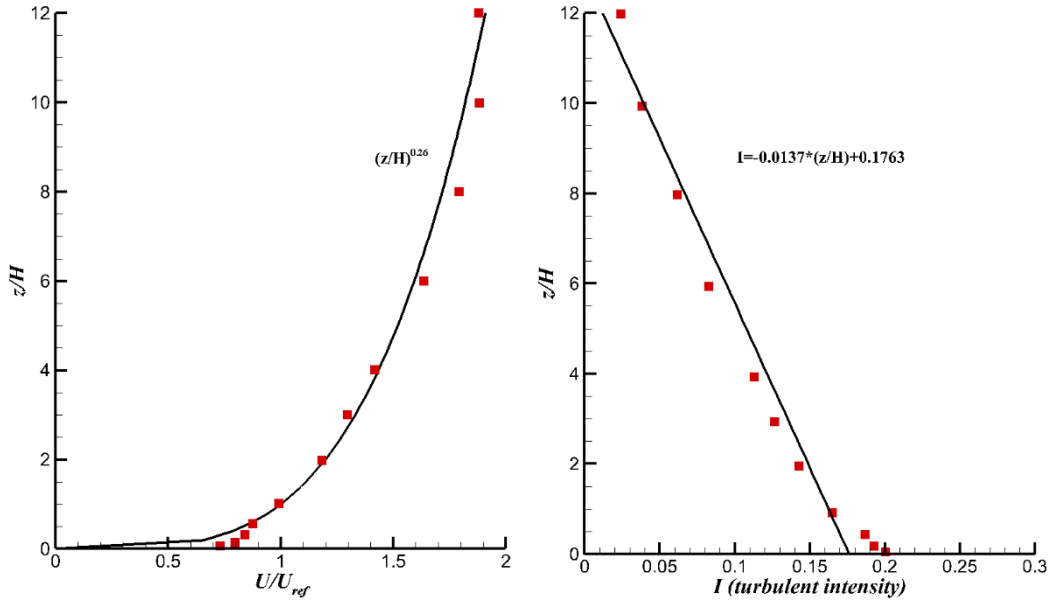

663 **(a)** **(b)**

664 **Fig. 3**. Comparisons of CFD inlet velocity (a) and turbulent intensity (b) profiles with
665 measurements from Tominaga and Stathopolous (2011).
666

Figure 4

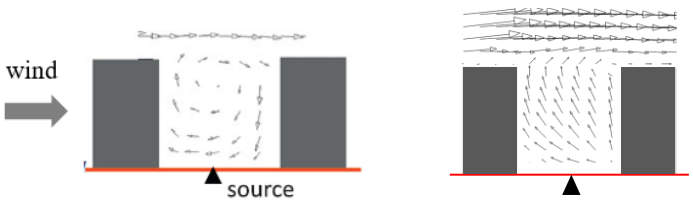

EXP Tominaga et al., (2011) Present study

(a)

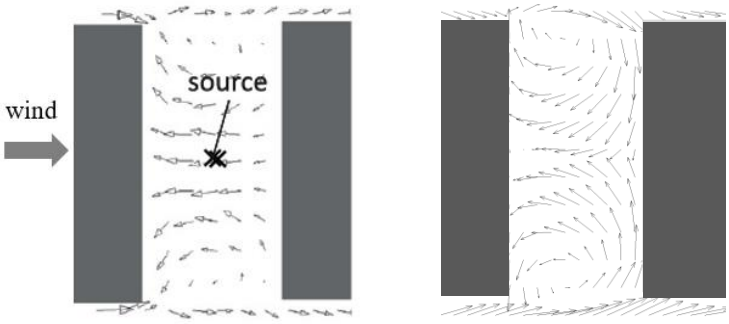

EXP Tominaga et al., (2011) Present study

(b)

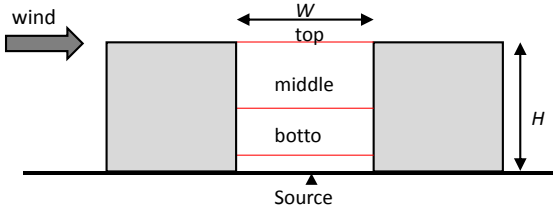

(c)

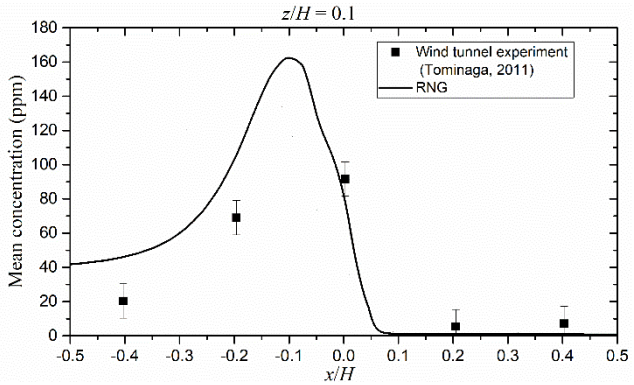

(d) Bottom line (z/H = 0.1)

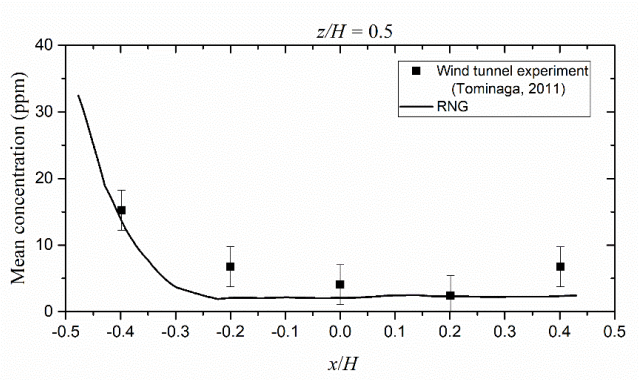

(e) Middle line (z/*H* = 0.5)

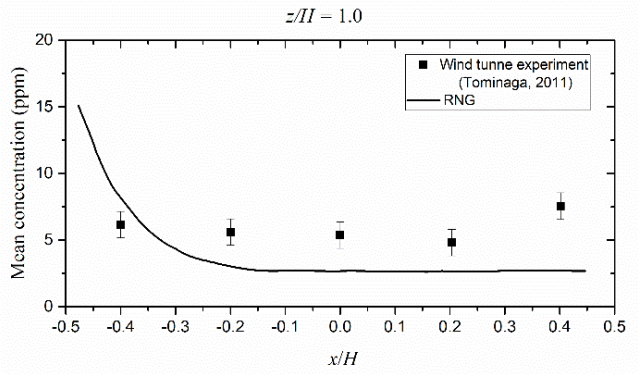

(f) top line (z/*H* = 1.0)

Fig. 4. Comparation of time-averaged concentration *c* inside a street canyon at three different heights of the symmetrical plane between the present RNG *k*-ε simulation and previous wind tunnel experiment.

Figure 5

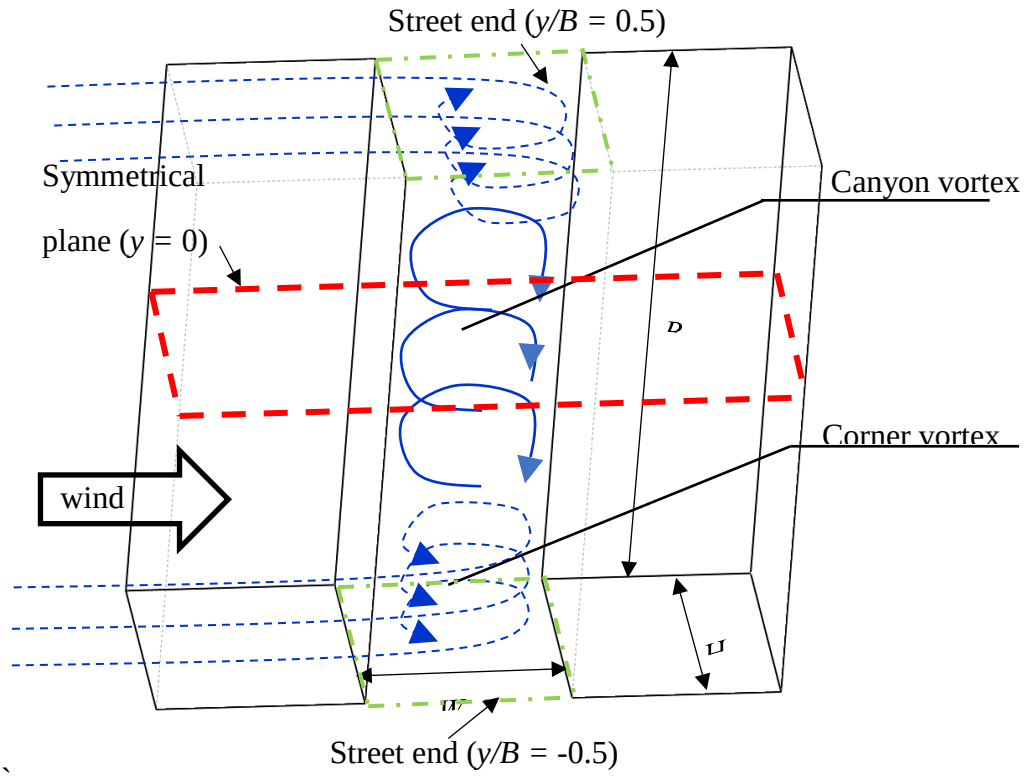

Fig. 5. Schematic illustration of the flow pattern within a 3-D street canyon surrounded by urban buildings and subjected to perpendicular approaching wind. The location of street ends and symmetrical planes are presented. The wind blows from the left to the right.

712 Figure 6
713
714
715
716
717
718
719
720
721

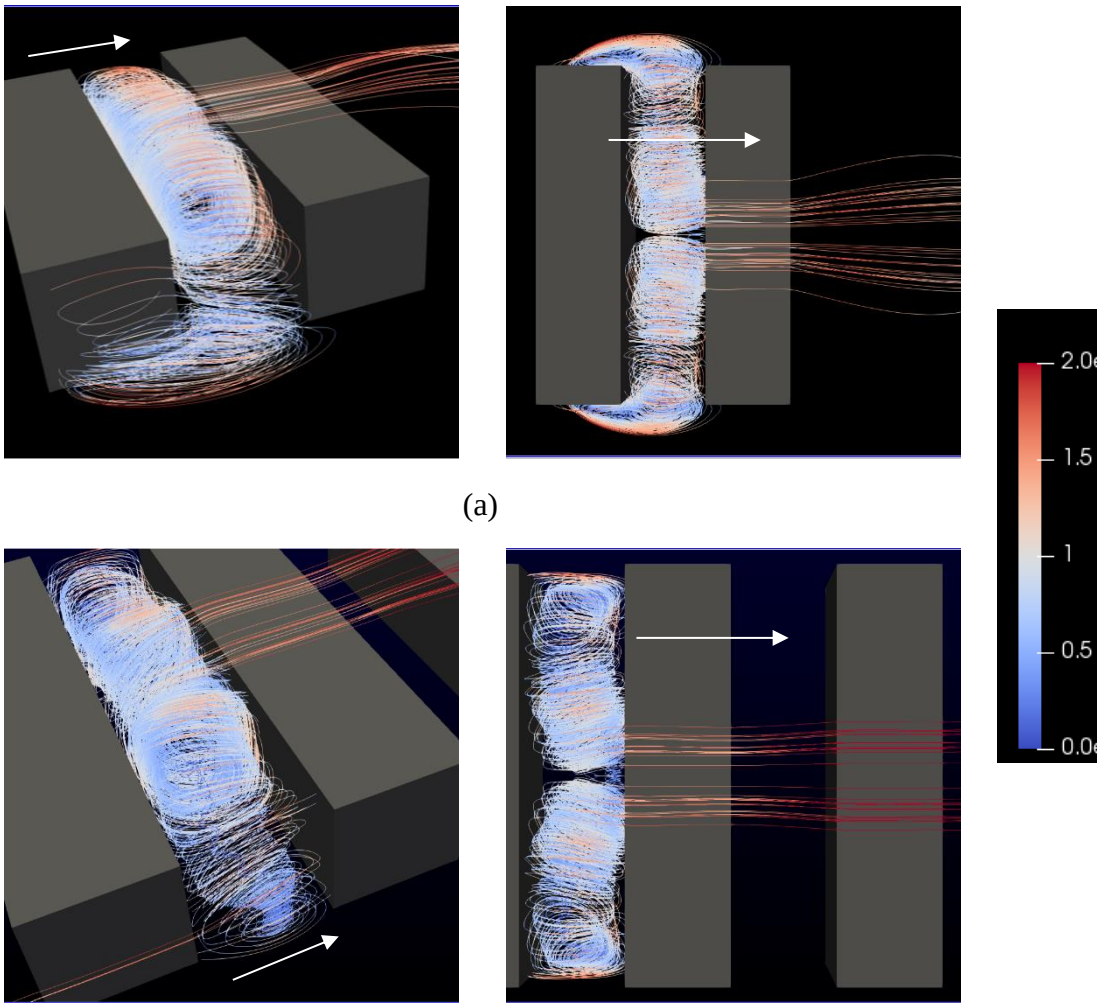

(a)

(b)

722 **Fig. 6**. 3-D streamline in street canyons with (H/W = 1.0, B/W = 4.0) for isolated street
723 canyon (a) and multiple canyons (b). The streamlines are coloured by mean velocity.
724 Streamlines are originated from multiple seed locations on a straight line above the line
725 source (z/H = 0.1). The ambient wind blows from the left to the right.
726
727

Figure 7

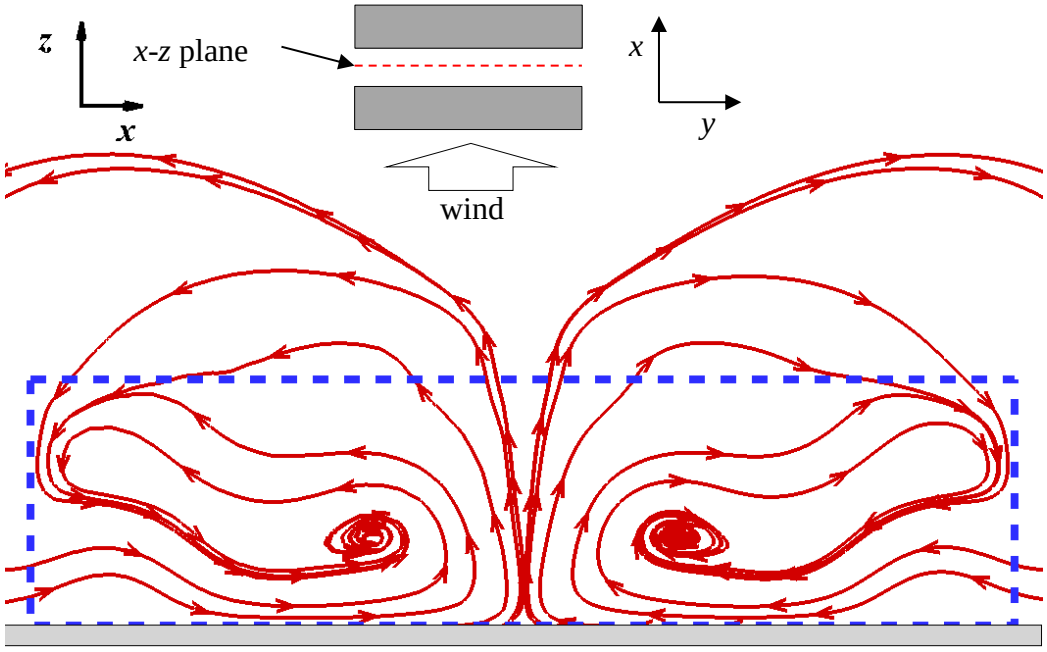

Fig. 7. Filtered streamlines plotted at the vertical plane (*x*-*z* plane, located at the street centreline, shown as red dash) for cases with H/W = 1 and B/W = 4. Noted that the *x*-velocity was filtered as zero at that plane to transfer 3D streamlines into 2D streamlines.

Figure 8

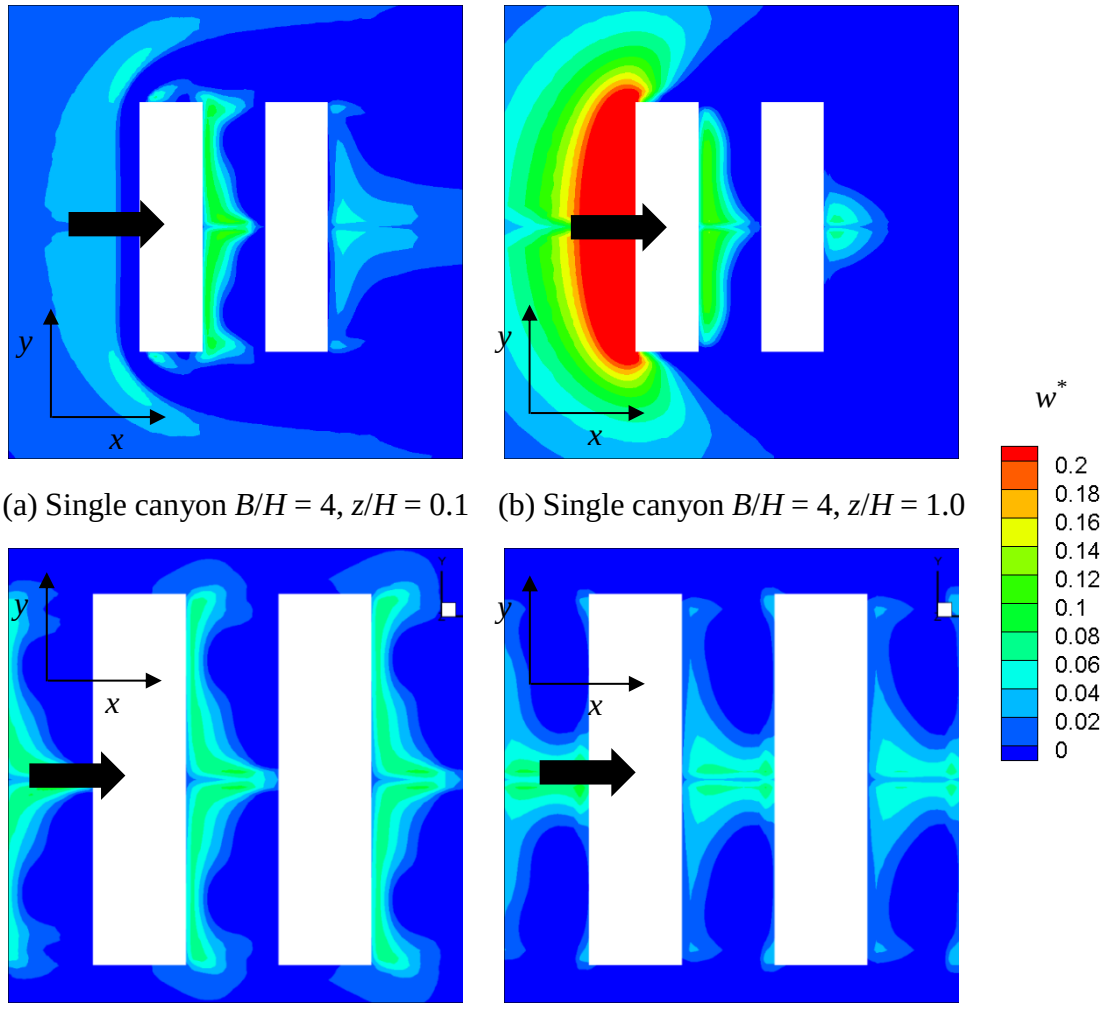

(a) Single canyon B/H = 4, z/H = 0.1

(b) Single canyon B/H = 4, z/H = 1.0

(c) Multiple canyon B/H = 4, z/H = 0.1

(d) Multiple canyon B/H = 4, z/H = 1.0

Fig. 8. The normalized mean vertical velocity $w^* = w/U_{ref}$ at two different height of z = 0.1H and 1.0H for cases with H/W = 1 and B/W = 4. The ambient wind blows from the left to the right.

Figure 9

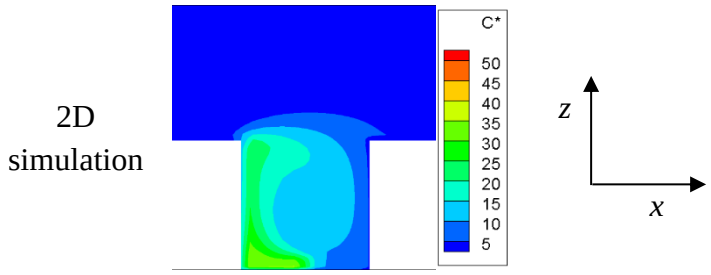

Slices at different positions from 3-D simulation			
B/*W*	*y*/*B* = 0	*y*/*B* = 0.25	*y*/*B* = 0.45
4			
10			
30			
60			

Fig. 9. Normalized pollutant concentration at 2-D simulation and *y*-planes for 3-D street canyon with isolated canyon and *H*/*W* = 1.0. The ambient wind blows from the left to the right.

Figure 10

2-D simulation

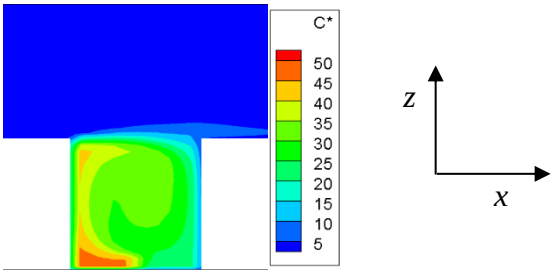

Slices at different positions from 3-D simulation			
B/*W*	*y*/*B* = 0	*y*/*B* = 0.25	*y*/*B* = 0.45
4	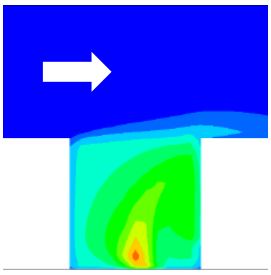	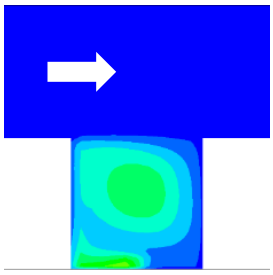	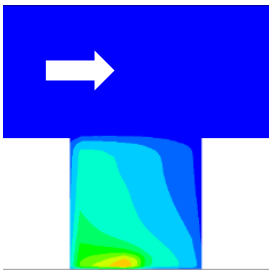
10	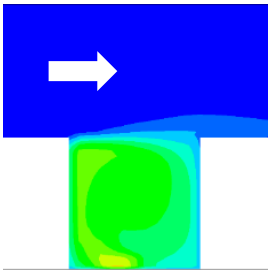	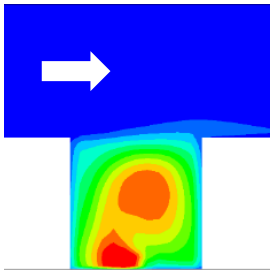	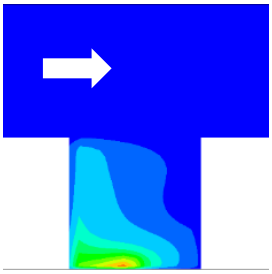
30	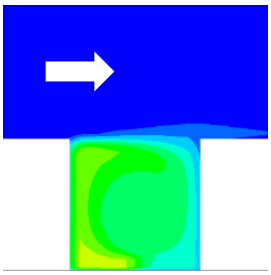	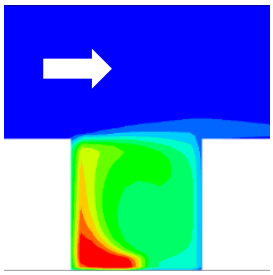	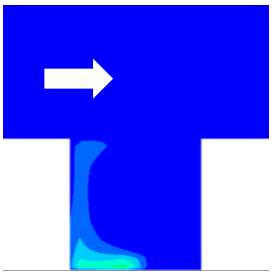
60	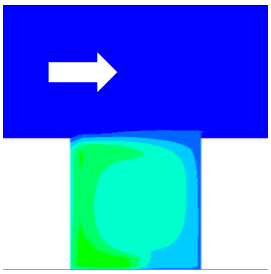	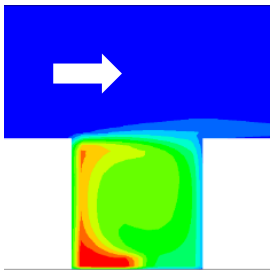	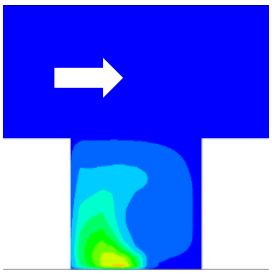

Fig. 10. Normalized pollutant concentration at 2-D simulation and *y*-planes for 3-D street canyon with multiple canyon and *H*/*W* = 1.0. The ambient wind blows from the left to the right.

Figure 11

776

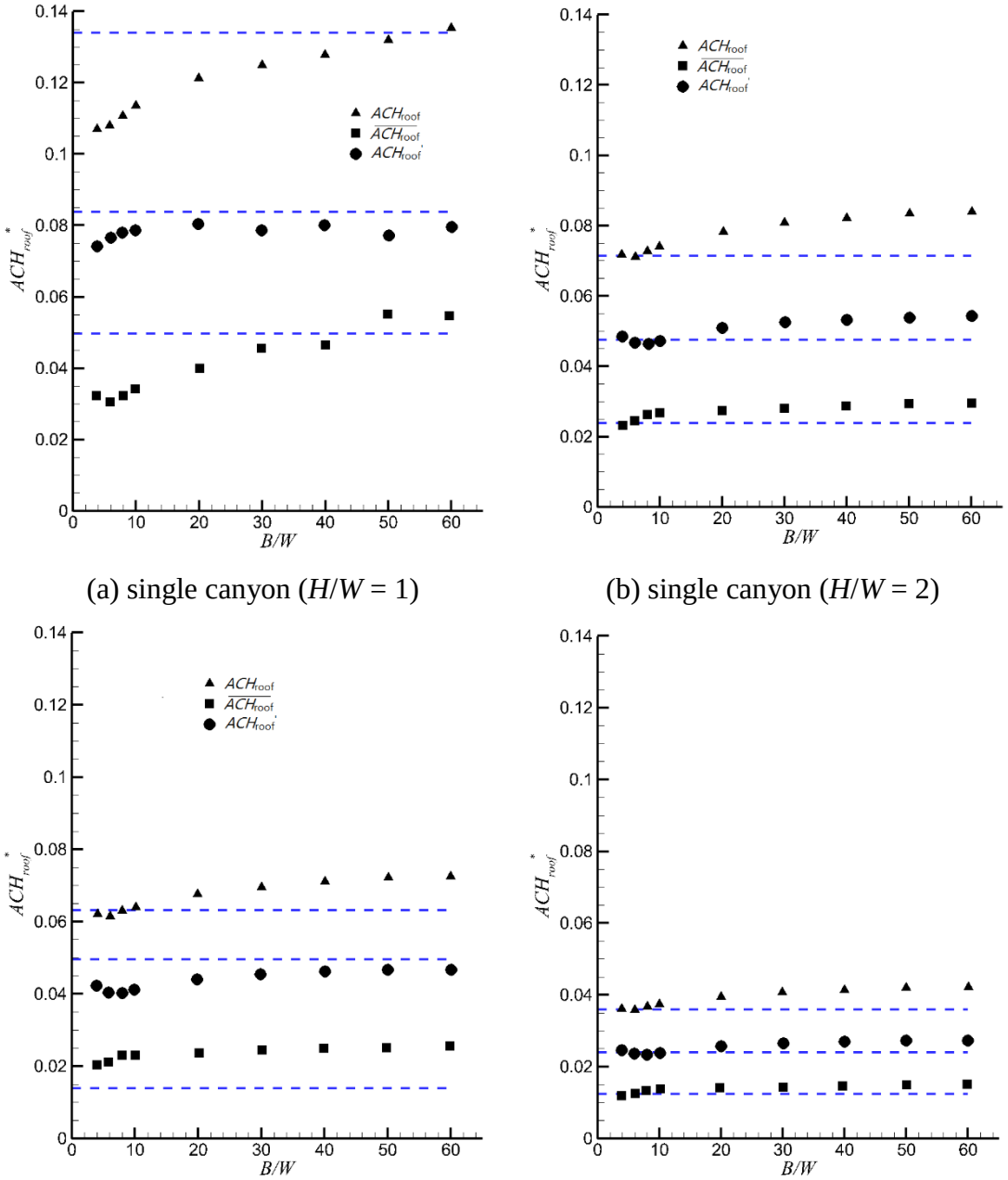

(a) single canyon (H/W = 1)

(b) single canyon (H/W = 2)

(c) Multiple canyon (H/W = 1)

(d) Multiple canyon (H/W = 2)

777 **Fig. 11**. Relationship between street length (B/W) and the overall air exchange rate (

778 ACH_{roof}), mean exchange rate ($\overline{ACH_{roof}}$) and turbulent exchange rate (ACH'_{roof}) at the roof.

779 The air exchange rates are normalized as ACH^* (= ACH/U_{ref}). The results of 2-D

780 simulation are plotted as blue dash lines.

781 Figure 12

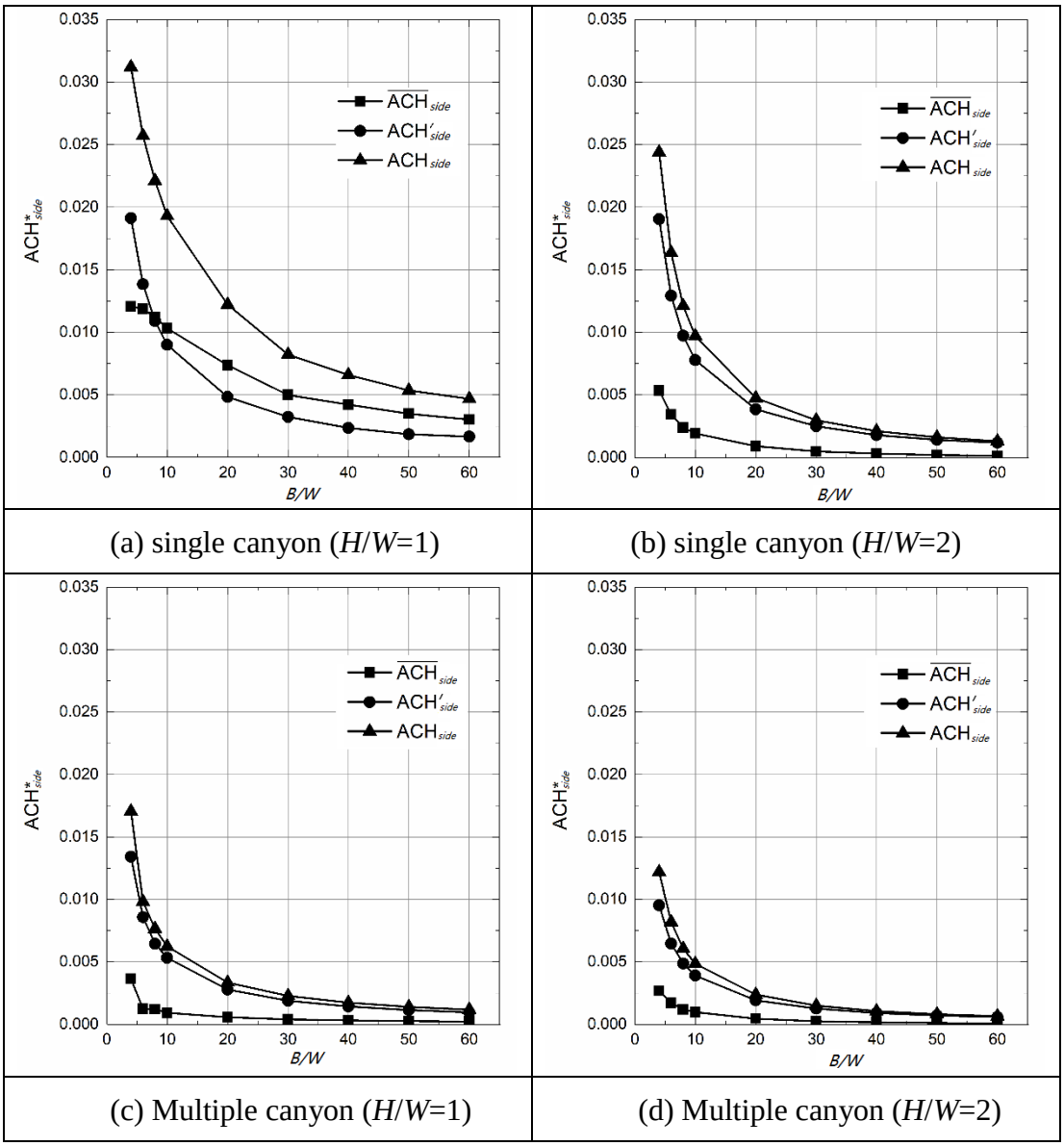

(a) single canyon (*H*/*W*=1) (b) single canyon (*H*/*W*=2)

(c) Multiple canyon (*H*/*W*=1) (d) Multiple canyon (*H*/*W*=2)

Fig. 12. Relationship between street length (*B/W*) and the overall air exchange rate (ACH_{side}), mean exchange rate ($\overline{ACH_{side}}$) and turbulent exchange rate (ACH'_{side}) at the street ends. The air exchange rates are normalized as ACH^* (= ACH/U_{ref}). The results of 2-D simulation are plotted as blue dash lines.

Figure 13

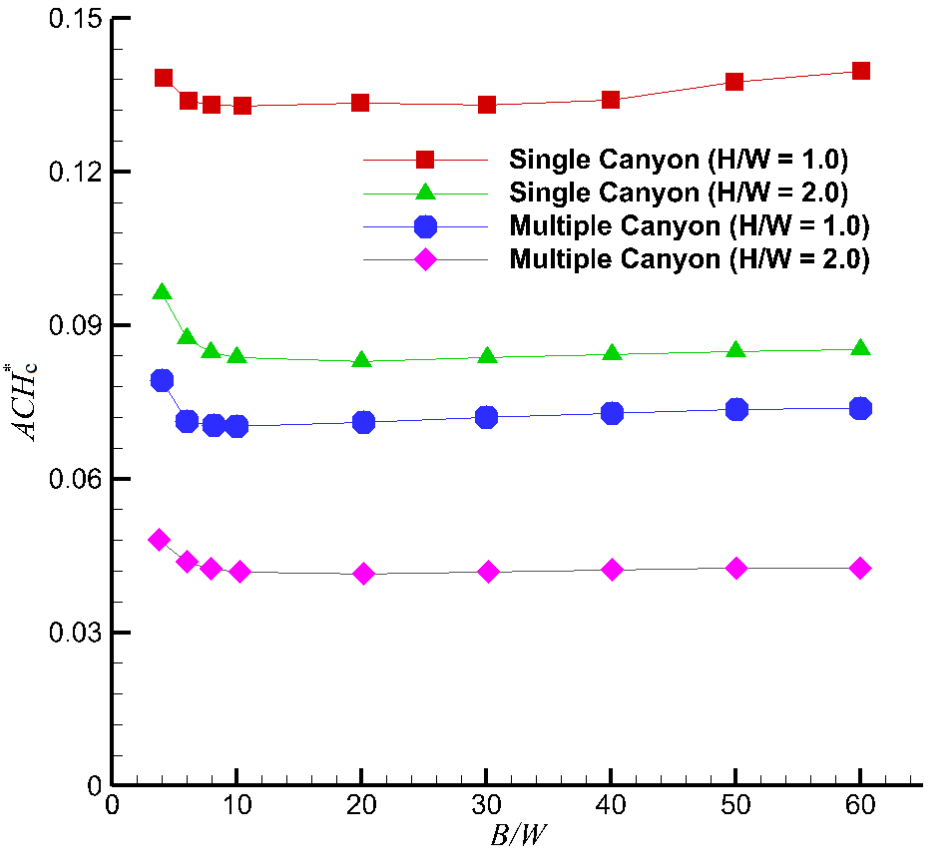

Fig. 13. The overall air exchange rate (ACH_c^*) of the whole street canyon against B/W (B the street length, W the street width).

812 Figure 14

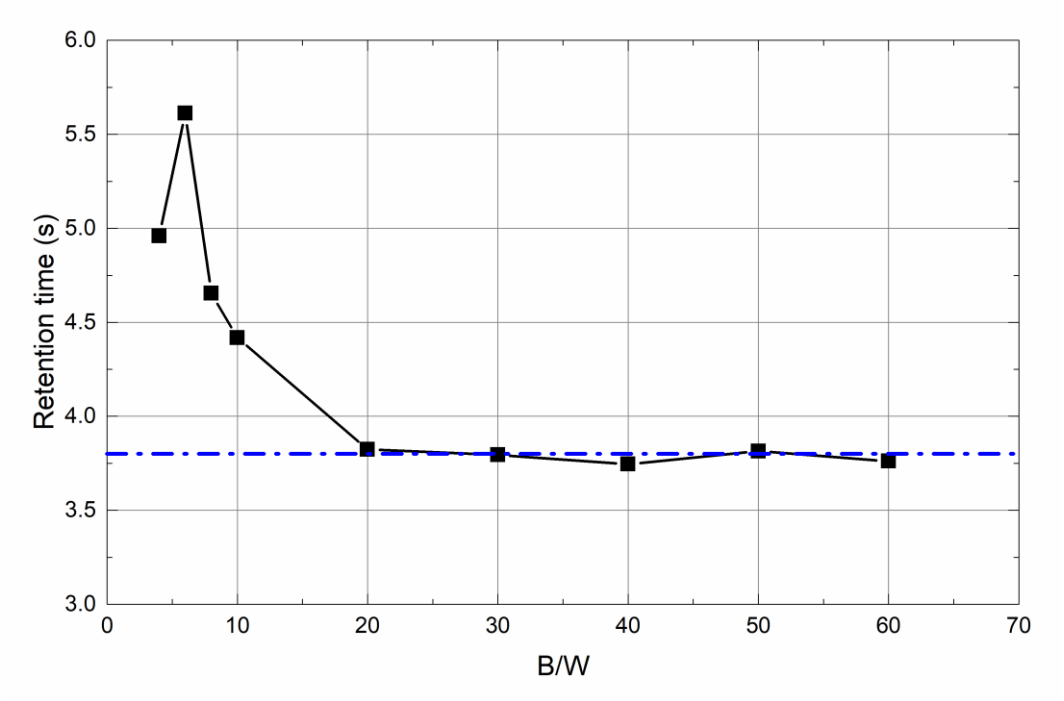

813

814 (a) Isolated canyon (H/W = 1.0)

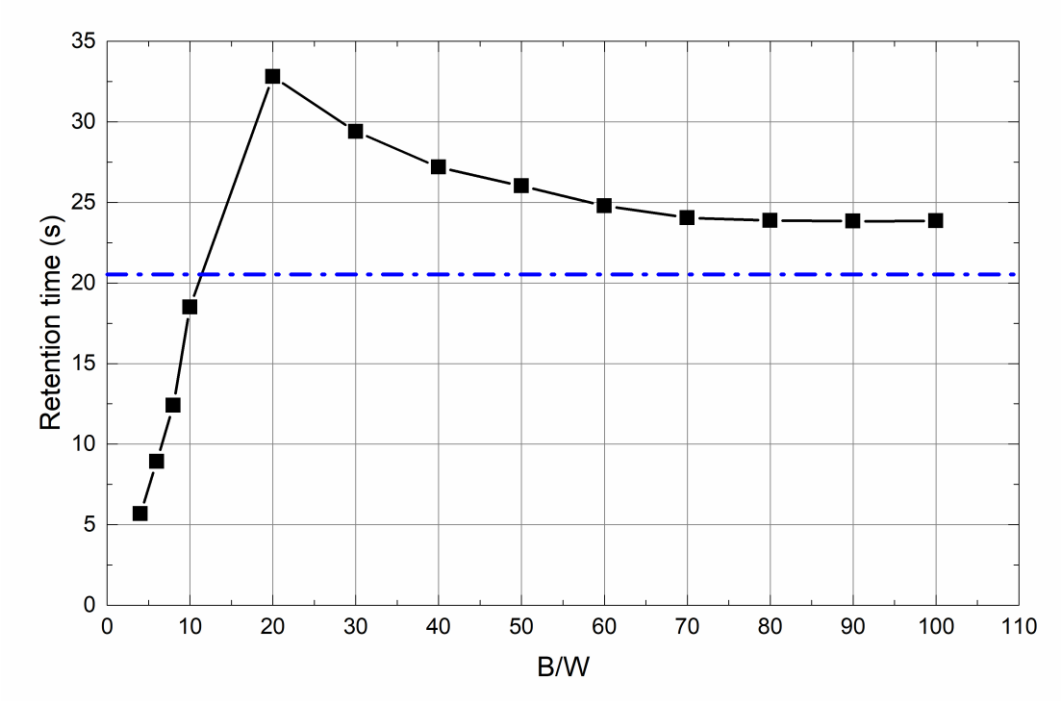

815

816 (b) Isolated canyon (H/W = 2.0)

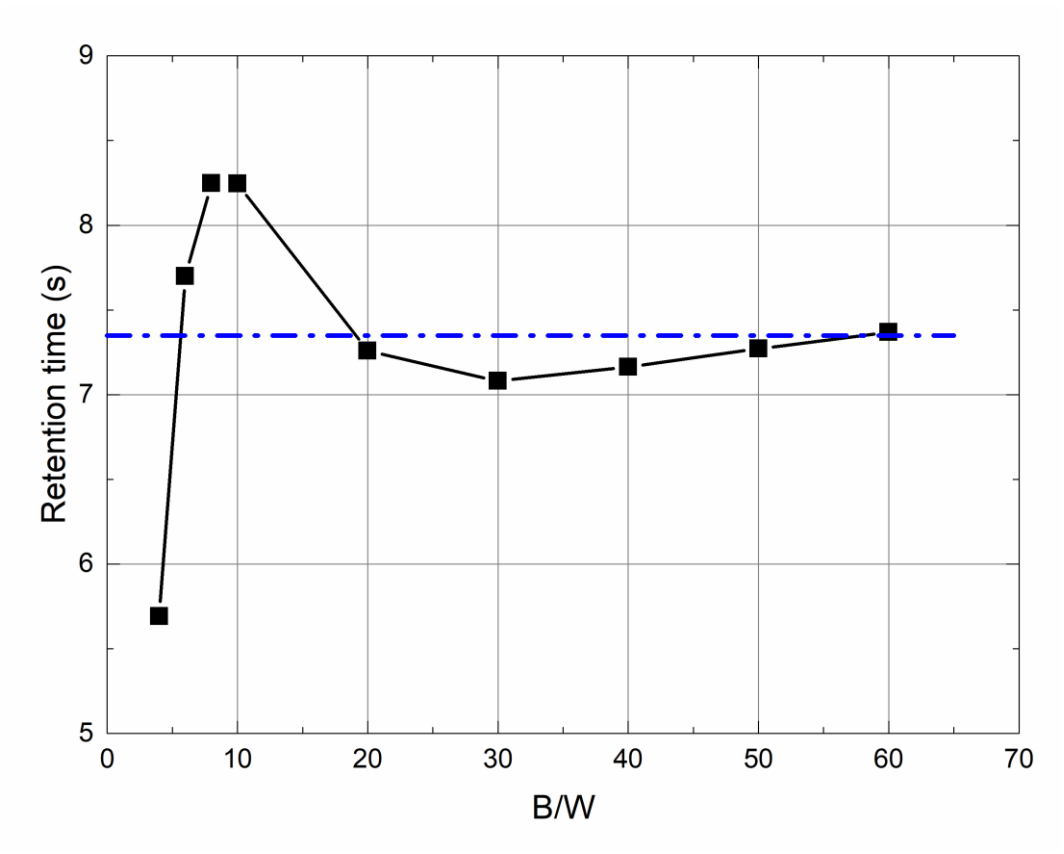

(c) Multiple canyon (H/W = 1.0)

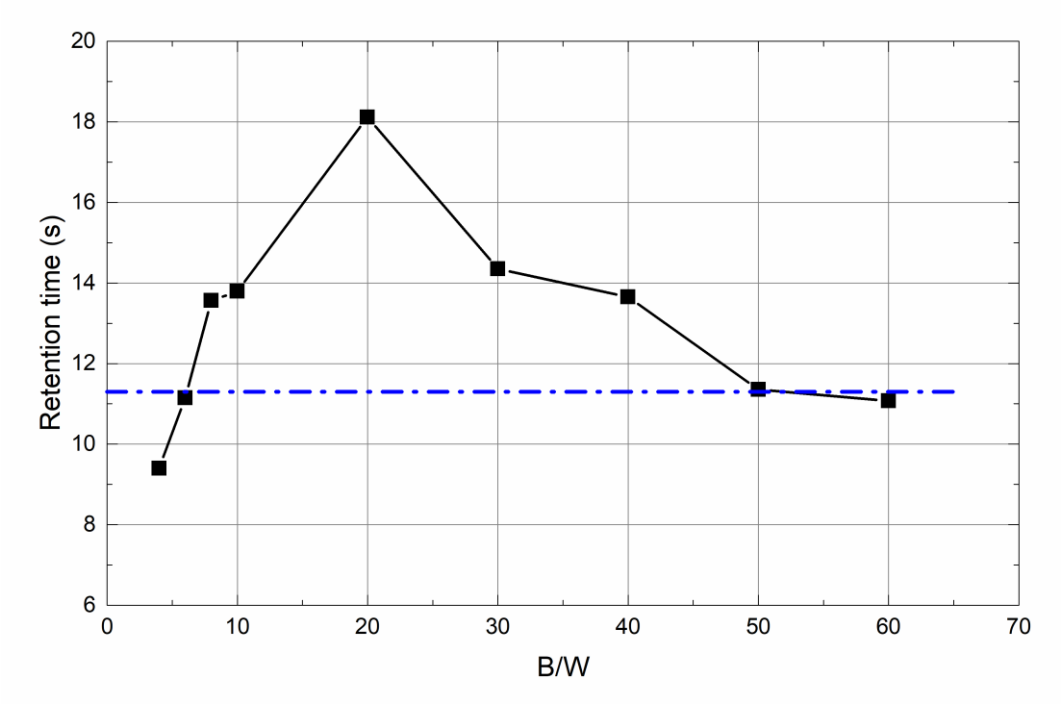

(d) Multiple canyon (H/W = 2.0)

Fig. 14. Canyon retention time τ_c against street length B/W.

Figure 15

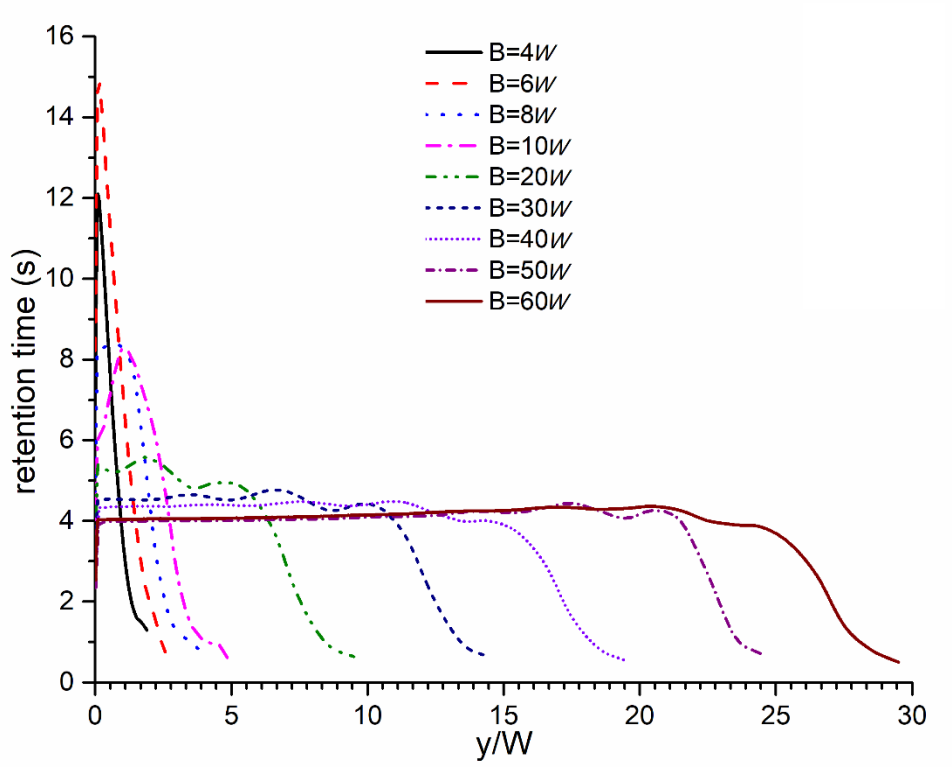

(a) Isolated canyon (H/W = 1.0)

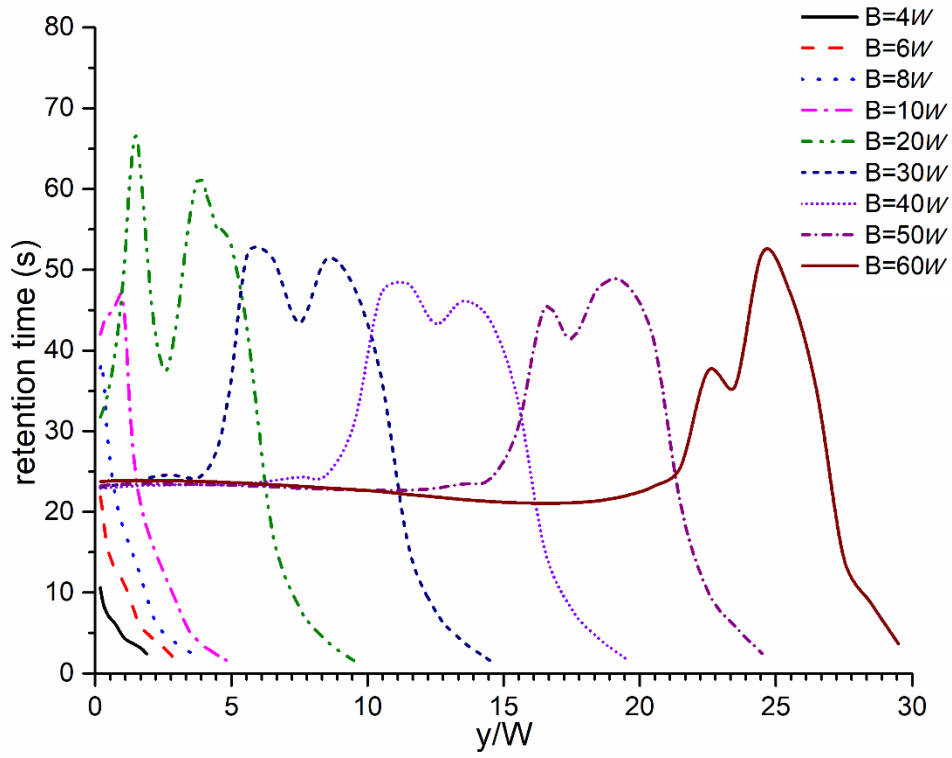

(b) Isolated canyon (H/W = 2.0)

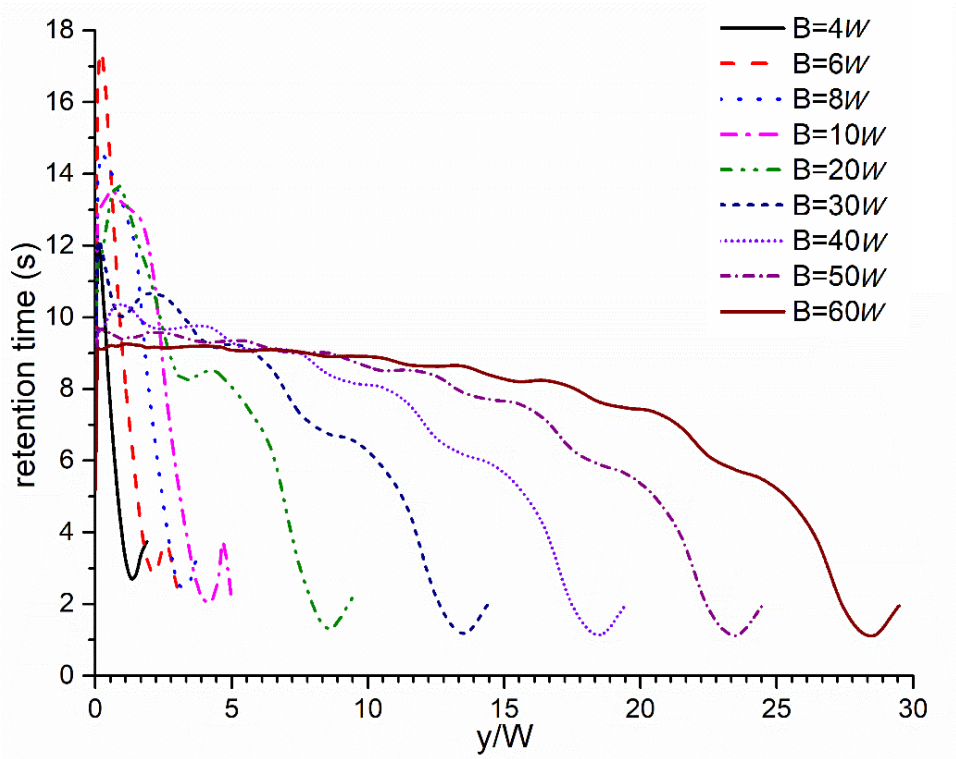

(c) Multiple canyon (H/W = 1.0)

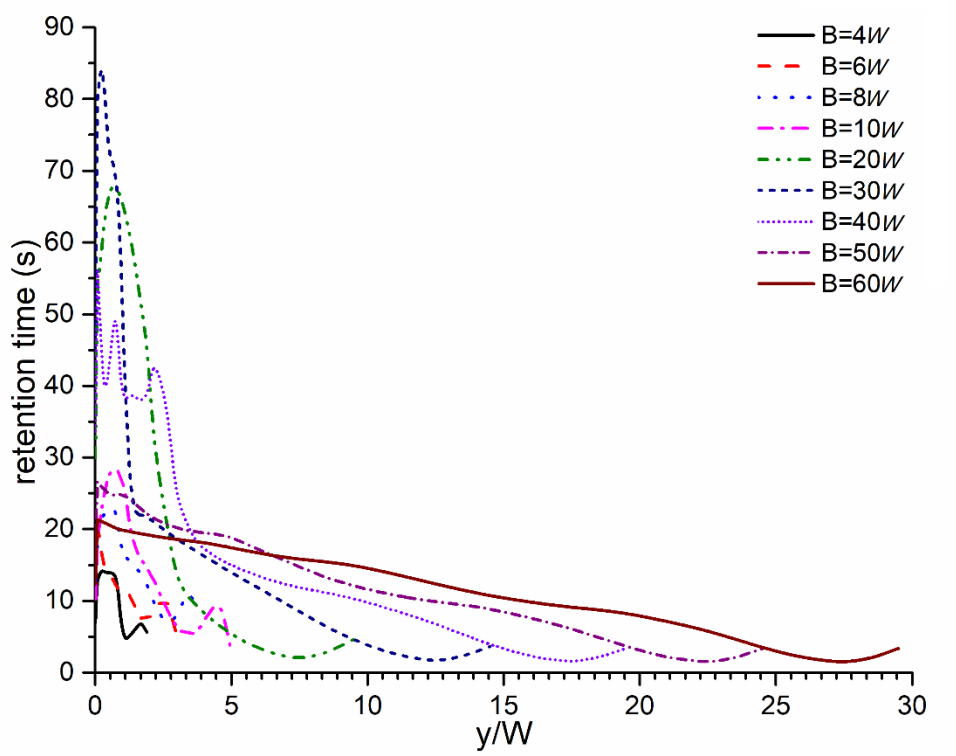

(d) Multiple canyon (H/W = 2.0)

Fig. 15. Distribution of averaged retention time along street direction (y-direction).